USGS
science for a changing world

Improved Automated Identification and Mapping of Iron Sulfate Minerals, Other Mineral Groups, and Vegetation using Landsat 8 Operational Land Imager Data, San Juan Mountains, Colorado, and Four Corners Region

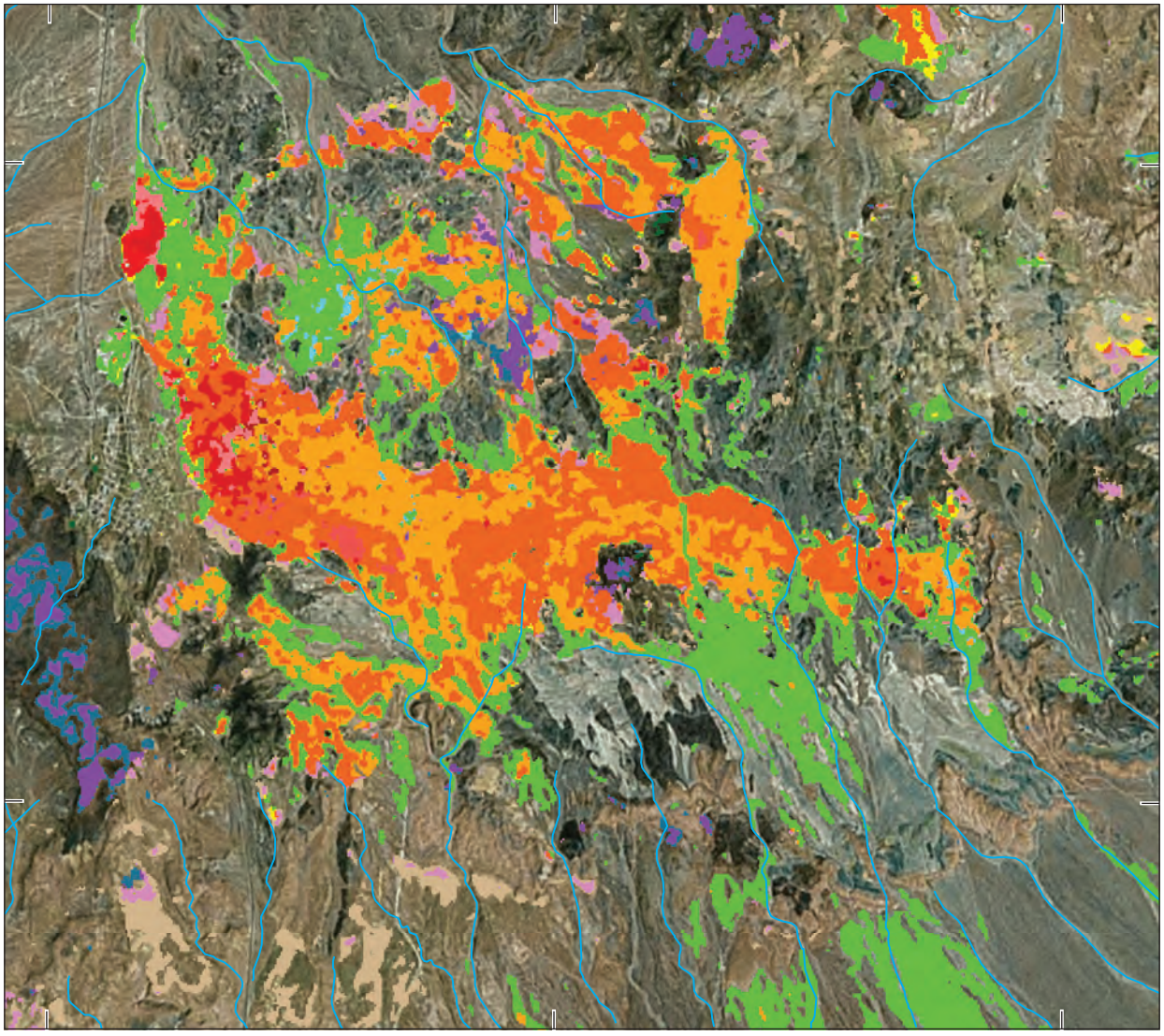

Pamphlet to accompany

Scientific Investigations Map 3466

U.S. Department of the Interior
U.S. Geological Survey

Front cover.—Mineral and vegetation group map of the Goldfield mining district, Nevada, generated from Landsat 8 OLI data using the automated algorithm described in this report.

Improved Automated Identification and Mapping of Iron Sulfate Minerals, Other Mineral Groups, and Vegetation using Landsat 8 Operational Land Imager Data, San Juan Mountains, Colorado, and Four Corners Region

By Barnaby W. Rockwell, William R. Gnesda, and Albert H. Hofstra

Pamphlet to accompany
Scientific Investigations Map 3466

U.S. Department of the Interior
U.S. Geological Survey

U.S. Geological Survey, Reston, Virginia: 2021

Suggested citation:
Rockwell, B.W., Gnesda, W.R., and Hofstra, A.H., 2021, Improved automated identification and mapping of iron sulfate minerals, other mineral groups, and vegetation using Landsat 8 Operational Land Imager data, San Juan Mountains, Colorado, and Four Corners Region: U.S. Geological Survey Scientific Investigations Map 3466, 1 sheet, scale 1:325,000, 37-p. pamphlet, https://doi.org/10.3133/sim3466.

Associated data for this publication:
Rockwell, B.W., and Gnesda, W.R., 2021, Digital map of iron sulfate minerals, other mineral groups, and vegetation of the San Juan Mountains, Colorado, and Four Corners Region derived from automated analysis of Landsat 8 satellite data: U.S. Geological Survey data release, https://doi.org/10.5066/P9ONOKKX.

ISSN 2329-132X (online)

Contents

Abstract....1
Introduction....1
Map and Data Characteristics....2
Map Usage....2
Descriptions of Map Sheet and Associated ERDAS Imagine Raster Image File Included in This Publication....4
PDF Map Sheet....4
Raster Image....4
Other Data in the PDF Map Sheet....4
Description of Automated Analysis Methodology....4
Mineral Group and Green Vegetation Indices....6
Iron Sulfate Mineral Index....6
Image Processing for Masking and Index Thresholding....8
Dark Area Masking....8
Water Masking....8
Final Index Thresholding and Clipping....8
Modeling of Mineral Groups through Boolean Combination of Index Results....10
Discussion of Regional-Scale Mapped Mineral Zonation Patterns....16
Discussion of Deposit-Scale Mapped Mineral Zonation Patterns....21
Deficiencies of the Automated Analysis Methodology....33
Conclusions....33
Acknowledgments....34
References Cited....34

Map Sheet

1. Improved Automated Identification and Mapping of Iron Sulfate Minerals, Other Mineral Groups, and Vegetation using Landsat 8 Operational Land Imager Data, San Juan Mountains, Colorado, and Four Corners Region, available for downloading from https://doi.org/10.3133/sim3466.

Figures

1. Reflectance spectra of ferric iron minerals showing the VIS, NIR, and SWIR regions (from Clark and others, 2007)....7
2. Plot of ferric iron mineral spectra from figure 1 convolved to Landsat 8 OLI spectral resolution....9
3. Color-coded explanation of analysis results produced by the algorithm presented herein....15
4. Laboratory reflectance spectrum of a sample of playa surface from northern Grass Valley, Lander County, Nevada....16
5. Comparison of map products generated by Landsat 8 data analysis and Landsat 7 data analysis....18

6. Mineral and vegetation group map of the Goldfield mining district, Nevada, generated from Landsat 8 OLI data using the automated algorithm described herein....22
7. Uncorrected Landsat 8 OLI spectra from scene covering Goldfield, Nevada, collected on August 1, 2013....24
8. Laboratory reflectance spectra of field samples collected from undisturbed, highly altered rock east of Diamond Peak in the Goldfield mining district, Nevada....25
9. Mineral maps of the Bauer Mill site near Stockton, Utah, derived from analysis of Landsat 8 OLI data and high-altitude AVIRIS data....27
10. Average spectra of Landsat 8 OLI data from tailings deposits at the Bauer Mill site....29
11. Average spectra of high-altitude AVIRIS data from tailings deposits at the Bauer Mill site sampled from the same general locations as the spectra in figure 10....30
12. Mineral group map of the northern Marysvale volcanic field, Utah, generated from Landsat 8 OLI data using the automated algorithm described herein....31

Tables

1. Generalized guide for preliminary interpretation of mineral group maps....3
2. Landsat 8 OLI reflective spectral data characteristics used for this study....5
3. Material indices used for analysis of Landsat 7 and Landsat 8 data, showing respective band designations for the two sensors....6
4. Boolean logic used to combine Landsat 8 ratio-based index results into the single, classified map shown on map sheet....11
5. Inductively coupled plasma mass spectrometry (ICP-MS) acid digestion results for a sample of playa surface from northern Grass Valley, Nevada....17

Conversion Factors

U.S. customary units to International System of Units

Multiply	By	To obtain
	Length	
inch (in.)	2.54	centimeter (cm)
inch (in.)	25.4	millimeter (mm)
foot (ft)	0.3048	meter (m)
mile (mi)	1.609	kilometer (km)
yard (yd)	0.9144	meter (m)

International System of Units to U.S. customary units

Multiply	By	To obtain
	Length	
centimeter (cm)	0.3937	inch (in.)
millimeter (mm)	0.03937	inch (in.)
meter (m)	3.281	foot (ft)

Multiply	By	To obtain
kilometer (km)	0.6214	mile (mi)
meter (m)	1.094	yard (yd)

Datum

Vertical and horizontal coordinate information is referenced to the World Geodetic System 1984 (WGS 84).

Altitude, as used in this report, refers to distance above the vertical datum.

Abbreviations

ASTER	Advanced Spaceborne Thermal Emission and Reflection Radiometer
AVIRIS	Airborne Visible/Infrared Imaging Spectrometer
DN	digital number
ERDAS	Earth Resources Data Analysis System
EROS	Earth Resources Observation and Science Center
ETM+	Enhanced Thematic Plus
FGDC	Federal Geographic Data Committee
GIFOV	ground instantaneous field of view
GIS	geographic information systems
HyMap	hyperspectral imaging sensor
ICP-MS	Inductively Coupled Plasma Mass Spectrometry
L1T	Landsat Level 1 Terrain (L1T) Correction
NAP	estimated relative degree of Net Acid Production
OLI	Operational Land Imager
QSP	quartz-sericite-pyrite
SWIR	shortwave-infrared
TM	Thematic Mapper
USGS	U.S. Geological Survey
UV	ultraviolet
VIS	visible
VNIR	visible to near-infrared
XRD	x-ray powder diffraction

Improved Automated Identification and Mapping of Iron Sulfate Minerals, Other Mineral Groups, and Vegetation using Landsat 8 Operational Land Imager Data, San Juan Mountains, Colorado, and Four Corners Region

By Barnaby W. Rockwell,[1] William R. Gnesda,[2] and Albert H. Hofstra[2]

Abstract

Multispectral remote sensing data acquired by the Landsat 8 Operational Land Imager (OLI) sensor were analyzed using a new, automated technique to generate a map of exposed mineral and vegetation groups in the western San Juan Mountains, Colo., and the Four Corners Region of the United States. Band ratio results were combined into displayed mineral and vegetation groups using Boolean algebra. New analysis logic has been implemented to exploit the coastal aerosol band in Landsat 8 OLI data and identify concentrations of iron sulfate minerals. These may indicate the presence of near-surface pyrite, which can be a potential nonpoint source of acid rock drainage. Zoned occurrences of iron sulfate minerals in areas surrounding and down gradient of known sources of pyrite have been mapped using this technique. They show high correlation with occurrences of jarosite-bearing mineral assemblages, as mapped using airborne imaging spectrometer data and supporting field verification surveys. Mapping the occurrence of iron sulfate minerals produced by the weathering and oxidation of pyrite in exposed hydrothermally altered rocks can also provide an important indicator of the genetic environment of alteration and the associated mineral deposit type. The automated analysis methodology is being employed to rapidly and cost-effectively generate maps of large regions of the United States in support of U.S. Geological Survey mineral resource and mineral-environmental assessments. This map, which includes the ERDAS IMAGINE (.img) thematic raster format in the data release, has been attributed by pixel value with mineral and vegetation group classification data, which can be queried in most image processing and GIS software packages.

[1]Lakewood, Colo.

[2]U.S. Geological Survey.

Introduction

Ongoing U.S. Geological Survey (USGS) mineral resource and geoenvironmental assessments have utilized mineral maps derived from spectral analysis of remote sensing data to identify and characterize hydrothermally altered rocks and other surfaces with acid-producing or neutralizing potential (Day and others, 2016). Two- and three-dimensional patterns of mineralogic zonation within hydrothermally altered rocks are important factors in identifying potential occurrences of concealed mineral deposits (Vikre and others, 2016). Investigations at deposit and watershed scales have described the importance of sulfide-bearing altered rocks and mine waste as diffuse sources of acidic solutions that can transport metals into the hydrologic system (Yager and others, 2008; Schmidt and others, 2012). These rocks and waste materials may contain minerals that can be identified using spectral analysis of airborne and satellite remote sensing data. Analysis of multispectral data acquired by the Advanced Spaceborne Thermal Emission and Reflection Radiometer (ASTER) and Landsat 7 Enhanced Thematic Plus (ETM+) sensors has been employed to generate mineral group maps over large areas of the United States (U.S.) and its territories in support of USGS assessment efforts (Rockwell, 2012, 2013a; Mars, 2013; Rockwell and others, 2015).

Since the launch of the Landsat 4 satellite in 1982, the six bands of multispectral data collected by the Thematic Mapper (TM) sensor have been used to identify and map mineral groups and other features on the Earth's surface. Although maps generated by such analysis are less detailed than those derived from analysis of the nine reflective bands of ASTER data, they are nevertheless useful in identifying hydrothermally altered rocks and ferric iron-bearing mine waste and can be very efficiently produced at national scales. Landsat data are available at no cost worldwide, and one Landsat scene covers approximately the same area as nine ASTER scenes. A previous report (Rockwell, 2013a) introduced a new methodology for the automated analysis of Landsat 7 Enhanced Thematic Mapper Plus (ETM+) data that has been applied to 447 scenes

covering the conterminous United States. This report builds on that work by utilizing the newer Landsat 8 Operational Land Imager (OLI), which has an additional coastal/aerosol band, as well as narrower band widths than Landsat 7 ETM+ data used in the prior work (Rockwell, 2013a). This report is designed to mimic the previous report using the new Landsat 8 data. Therefore, relevant text from Rockwell (2013a) is reproduced herein to frame the presentation.

The OLI sensor on the Landsat 8 satellite launched on February 11, 2013, extends the legacy of the Landsat multispectral remote sensing program, by adding several important enhancements that considerably improve spectral mapping capabilities. These include (1) increased signal-to-noise ratios and 12-bit radiometric quantization, which increase the accuracy of surface feature discrimination, and (2) a new band in the visible (VIS) wavelength region designed for coastal and aerosol studies, which is ideally suited for more detailed discrimination of iron-bearing mineral species, since many iron minerals have diagnostic spectral absorption features in this wavelength region.

This report introduces a methodology for the automated analysis of Landsat 8 OLI data, adapted from the methodology for analyzing Landsat 7 ETM+ data as presented by Rockwell (2013a). A map of mineral groups and green vegetation produced using this same approach is presented, and covers the western San Juan Mountains of Colorado, and the Four Corners Region of Colorado, Utah, New Mexico, and Arizona. To test the validity and accuracy of this methodology, map results are compared to mineral and vegetation maps of the Silverton, Colorado region produced from analysis of Airborne Visible/Infrared Imaging Spectrometer (AVIRIS) data (Dalton and others, 2005, 2007) and ASTER data (Rockwell, 2012). The method has been applied to 216 scenes covering the western conterminous United States and selected additional areas with high mineral resource potential around the world.

The USGS National Map of Surficial Mineralogy (Rockwell and others, 2015) is an online map resource that presents maps of exposed surface mineral groups derived from Landsat 7 ETM+ (Rockwell, 2013a) and ASTER (Rockwell, 2012) satellite data covering the western conterminous United States, locations of significant mineral deposits (Long and others, 1998; Rockwell and Hofstra, 2008), and other geospatial data including maps of lithology and geologic structure derived from USGS State geologic maps, high-resolution imagery, topographic maps at scales up to 1:24,000, and hydrologic data. The online resource also includes more detailed surficial mineral maps derived from spectroscopic analysis of ASTER and hyperspectral data, including HyMap (airborne hyperspectral imaging sensor) and AVIRIS, over some important mining districts and mineralized areas. The inclusion of the different generations of maps makes it possible to directly compare the mineral mapping capabilities of the different sensors and analysis techniques, as well as the mineralogical expressions of mineral deposits and mine sites at a variety of spatial and spectral resolutions.

Map and Data Characteristics

The map presented here was produced from one full scene of Landsat 8 OLI data acquired on June 20, 2013. The Landsat data were obtained from the USGS Earth Resources Observation and Science Center (EROS) in L1T orthorectified format.

The results of digital mineral and vegetation mapping are presented in a multilayered, interactive, geospatial portable document format (PDF) and ERDAS Imagine format (.img). Georeferencing information is included in both file types. Multiple, geographically referenced map layers can be turned on and off for viewing and printing of the geospatial PDF files. Also included in the PDF files is a map of interpreted hydrothermal alteration types, mineral groups, and green vegetation derived from automated analysis of ASTER data (see layer "ASTER—Mineralogy + vegetation"; Rockwell, 2012; Rockwell and others, 2015), as well as preliminary lithologic and structural data derived from State geologic maps (see layer "Geologic Map"; Horton and others, 2017). Subsidiary map layers showing administrative boundaries, roads, surface hydrology, and landmarks (for example, National Parks in layer "Base Maps") are also included and can be opened via the PDF layers view. The ERDAS-format image is suitable for integration with other geospatial data in geographic information systems (GIS). The image shows occurrence of mineral and vegetation groups and has been attributed according to identified material type. This attribution enables interactive query and selection of color-coded material types using identification tools available in GIS and image processing software packages (for example, the Identify Tool of ArcMap and the Inquire Cursor Tool of ERDAS Imagine). For the attribute information to appear in the ArcMap Table of Contents, open the ERDAS file in ArcMap and symbolize using Unique Values for the "Materialid" value field. Federal Geographic Data Committee (FGDC)-compliant metadata have been included for the ERDAS-format file, and contain important information regarding geographic coordinate systems, attributes describing identified materials, and cross references to related reports. The ERDAS file and metadata are available as a data release in ScienceBase and can be found at https://doi.org/10.5066/P9ONOKKX (Rockwell and Gnesda, 2021).

Map Usage

The map layer was primarily designed to be used for regional mapping and characterization of exposed surface mineralogy, including that related to hydrothermal alteration and supergene weathering of pyritic rocks (Rockwell, 2012). The presence and type of alteration can be important information for use in mineral resource investigations since sericitic, advanced argillic, and intermediate argillic alteration commonly occurs along faults, fractures, or in permeable lithologies that serve as conduits for potentially metal-bearing fluids.

Prospective areas for epithermal and intrusion-related mineralization in which alteration is identified are, in general, more likely to host near-surface hydrothermal mineral deposits, although most altered rocks are barren of economic mineralization (Swayze and others, 2014).

Pyrite is a common gangue mineral in hydrothermal mineral deposits and may also occur in zones of hydrothermally altered rock surrounding these types of deposits. For this reason, mapping of the distribution of pyrite and its weathering products is an important part of geoenvironmental studies of mineral deposits (Seal and Foley, 2002). Weathering of pyrite upon exposure to atmospheric oxygen and water produces sulfuric acid. This can leach and transport potentially toxic metals into surface and groundwater systems. Knowledge of the occurrence of pyrite and other iron sulfide mineral phases and the extent and type of alteration is important in developing predictive models of downstream surface water geochemistry in both mined and unmined catchments, and in evaluating pre- and post-mining effects of alteration on local hydrology, fauna, and flora (Church and others, 2009; Schmidt and others, 2009). Ferric iron sulfate minerals including jarosite, copiapite, melanterite, and goethite are also produced during the weathering process. Large concentrations of such iron sulfate minerals can be identified using the analysis methodology for Landsat 8 data presented here. Concentrations of undifferentiated ferric and ferrous iron-bearing minerals can also be identified using Landsat 7 ETM+ (Rockwell, 2013a) and ASTER (Rockwell, 2012) data. Mine waste and tailings in which no iron-bearing mineral groups are mapped are less likely to represent exposed, nonpoint sources of acidic solutions. They may also have too small an area to be mapped using Landsat data, which have a ground resolution of 30 m per pixel. Where mine waste and mill tailings are of sufficient areal extent, the maps can also be used to evaluate mineral exposure at mine sites that have undergone remediation prior to the acquisition of the Landsat data. Importantly, note that maps of Landsat-based mineral groups are more effective for identifying potentially acid-producing assemblages than they are for identifying acid-neutralizing assemblages such as carbonates and chlorite. This is due to the weak spectral absorption features of CO_3^{2-} and Mg-OH molecules at Landsat TM spectral resolution.

The new Landsat 8 OLI analysis algorithm provides a cost-effective tool for geographically screening large areas for the presence of abundant iron sulfate minerals in mine waste, tailings, and hydrothermally altered rock. The algorithm also allows for the differentiation of quartz-sericite-pyrite (QSP or phyllic) alteration from undisturbed, pyrite-bearing magmatic-hydrothermal advanced argillic alteration in areas where alunite and (or) pyrophyllite are known to occur. This differentiation of alteration types is important for both mineral resource and geoenvironmental assessments because alteration types are associated with different types of mineral deposits, sulfide contents, and geoenvironmental models.

The Landsat 8 OLI-derived mineral-group map can be best interpreted in conjunction with geologic maps in a GIS. The character and origin of an identified mineral-group occurrence can be understood by recognizing the host rock lithology or material type (table 1). Most areas of known hydrothermal alteration contain the clay-sulfate-mica-marble mineral group (Rockwell, 2013a), but most mineral group occurrences are unrelated to alteration. Within un-metamorphosed volcanic rocks and most mine waste, the presence of alteration and (or) supergene weathering of pyrite can be inferred if both ferric iron and the clay-sulfate-mica-marble mineral groups are present, especially in the same pixel.

Table 1. Generalized guide for preliminary interpretation of mineral group maps.

[Modified from Rockwell and Hofstra (2012). Carbonate minerals are not reliably detected using the Landsat 8 OLI data analysis methodology, as explained in text below]

Host rock or material type	Highest-probability origin of mineral group occurrence
Volcanic	Hydrothermal alteration
Plutonic	Lithology (commonly mica) or alteration
Sedimentary	Lithology (commonly mica and (or) clays±carbonates), diagenesis, or alteration (rare, with an exception being dickite and (or) kaolinite in groundmass of quartzites and quartz arenites near intrusions)
Metamorphic	Lithology, weathering, metamorphic grade and type, or alteration (rare)
Alluvium	Weathering
Mine waste	Alteration and (or) supergene weathering of pyritic rocks

Descriptions of Map Sheet and Associated ERDAS Imagine Raster Image File Included in This Publication

PDF Map Sheet

The multilayered, interactive, geospatial PDF map sheet shows the results of a methodology designed for the automated identification and mapping of mineral groups and green vegetation from Landsat 8 OLI data. Detailed description of this methodology is provided in the following section. These results were modeled from the raw results of the ratio-based analysis algorithm, using Boolean algebra. In the map sheet explanation, the 19 output classes are ordered relative to decreasing inferred acid-producing potential in non-sedimentary rocks (commonly referred to as net acid production, or NAP). Note that although ferrous iron has little to no acid neutralizing capacity (ANC), it is often associated with chlorite-, epidote-, and (or) carbonate-bearing rocks including those with propylitic alteration that can have substantial ANC (Yager and others, 2008).

Raster Image

The ERDAS Imagine raster image included in the data release for this report (L8_P35R34_SilvertonCO.img, Rockwell and Gnesda, 2021) shows the spatial occurrence of mineral groups and dense green vegetation interpreted from Landsat 8 OLI data. This information can be used by geologists, watershed modelers, and land managers engaged in geoenvironmental watershed modeling or mineral resource assessment at regional to national scales. Each pixel in the image has been assigned an attribute with material identification data, which can be queried in most image processing and GIS software packages. The metadata within the data release (Rockwell and Gnesda, 2021) describe the identified mineral and vegetation groups portrayed in this image and attribute values assigned to the pixels contained in the image file.

Other Data in the PDF Map Sheet

In addition to the exposed surface and vegetation mineral map derived from analysis of Landsat 8 OLI data, the map sheet includes (1) several Landsat 8 color composite images, (2) a material map derived from analysis of Landsat 7 data (see layer “Landsat 7—Mineralogy + vegetation”; Rockwell, 2013a), (3) lithologic and structural data derived from State geologic maps (see layer “Geologic Map”; Horton and others, 2017), and (4) a mosaic of exposed surface and vegetation mineral maps derived from analysis of ASTER data (see layer “ASTER—Mineralogy + vegetation”; Rockwell, 2012; Rockwell and others, 2015). These additional data layers are included to enable easy, pixel-by-pixel comparisons with the Landsat 8 OLI-derived material map. Of particular interest is to highlight the improved mapping of iron sulfate-bearing groups of minerals by use of these new Boolean operators designed especially for use with Landsat 8 OLI data, as compared to those previously designed for use with Landsat 7 ETM+ data by Rockwell (2013a).

Description of Automated Analysis Methodology

Landsat 8 OLI multispectral data consist of nine bands measuring reflected electromagnetic energy (bands 1–9, 0.43–2.29 micrometers [μm]) and two bands measuring emissive thermal infrared energy (bands 10 and 11, 10.6–12.51 μm) (USGS, 2013). Only the reflective bands that have a ground instantaneous field of view (GIFOV, or ground pixel size) of 30 m, bands 1–7 (table 2), were used for this study. Band ratios highlight variation in reflectance between wavelength regions measured by the various bands of the sensor. They have been the simplest and most widely used analysis method applied to TM data (Crippen, 1989; Knepper, 1989, 2010; Rockwell, 1989, 2013a; Vincent, 1997).

Automated processing and analysis techniques are required to efficiently generate uniform maps of surficial mineralogy and green vegetation over large areas using Landsat data. The analysis must accurately identify exposed minerals or mineral groups (minerals having similar spectral properties given the spectral resolution of the data being analyzed) from any suitable Landsat scene in any climate or terrain with no operator interaction. Suitable scenes are those with minimal cloud, haze, dust, smoke, and snow cover and maximal solar illumination (high solar elevation angle, as occurs between late spring and early autumn).

In the northern hemisphere, scenes acquired in late May through early July are optimal to avoid the presence of senesced cheat grass (Bromus tectorum) and other dry vegetation that are more abundant in mid-summer through autumn (Kokaly, 2011). Such dry vegetation typically has deep absorptions in the shortwave-infrared (SWIR) region caused by leaf biochemicals such as lignin and cellulose (Elvidge and Lyon, 1985). These are spectrally similar at Landsat TM and OLI spectral resolution to minerals having strong SWIR (band 7) absorption features (Elvidge and Lyon, 1985; John and others, 2010). This spectral similarity of dry vegetation to many clay, sulfate, and mica minerals can lead to false identifications of this mineral group when Landsat scenes acquired in mid-July through October are analyzed, especially over areas in which invasive cheatgrass is abundant, such as the northern Great Basin (northern Nevada and surrounding region, extending eastward through northern Utah and into southern Wyoming).

Table 2. Landsat 8 OLI reflective spectral data characteristics used for this study.

[Modified from USGS (2013). Landsat 7 band characteristics shown for comparison; micrometers (μm); not applicable (NA)]

Band	Corresponding Landsat 7 ETM+ band number	Landsat 8 OLI wavelength range (μm)	Landsat 7 ETM+wavelength range (mm)	Landsat 8 OLI band center (μm)	Landsat 7 ETM+ band center (μm)	Landsat 8 OLI Bandwidth (μm)	Landsat 7 ETM+ Bandwidth (μm)	Wavelength region
1	NA	0.43–0.45	NA	0.44	NA	0.02	NA	Ultra–blue, coastal aerosol
2	1	0.45–0.51	0.45–0.52	0.48	0.485	0.06	0.07	Blue
3	2	0.53–0.59	0.52–0.60	0.56	0.56	0.06	0.08	Green
4	3	0.64–0.67	0.63–0.69	0.655	0.66	0.03	0.06	Red
5	4	0.85–0.88	0.77–0.90	0.865	0.83	0.03	0.14	Near–infrared (nir)
6	5	1.57–1.65	1.55–1.75	1.61	1.65	0.08	0.2	Shortwave–infrared (swir) 1
7	7	2.11–2.29	2.09–2.35	2.2	2.215	0.18	0.27	Shortwave–infrared (swir) 2

The processing methodology presented here outlines the use of compound band ratios to identify areas where one or more specific spectral absorption features are present. Ratios were developed to identify mineral groups based on diagnostic absorptions of pure and mixed mineral species in laboratory reference spectra that were resampled to Landsat 8 OLI spectral resolution. The technique assumes that only a particular mineral or mineral group (or green vegetation) will have deep absorption at a particular wavelength interval (one or more adjacent Landsat bands). If another surface material, material mixture, or feature has deep absorption at a given wavelength interval, a false detection of a mineral group having a similar absorption feature will occur. The utility of a ratio of type (x + y) / z to identify absorption at band z relative to adjacent bands x and y was first demonstrated by Crowley and others (1989), who described the technique of relative band depth mapping.

Prior to computing the material indices described below, the uneven edges of the Landsat TM bands were equalized by setting pixels to zero if that pixel had a digital number (DN) value of zero in any band in the raw data. To mitigate the effects of Rayleigh (gaseous) scattering, a dark-target subtraction was applied following Kaufman (1989):

$$DN_{haze} = DN_{raw} + (C - DN_{min}) \quad (1)$$

where

DN_{haze} is the haze corrected value for gaseous scattering;
DN_{raw} is the raw measured value;
C is the nonzero minimum value per band; and
DN_{min} is the nonzero minimum digital number value per band.

A C value of 5 was used to avoid divisions by zero in the ratio-based analysis. Similar atmospheric corrections using dark-target subtraction were discussed by Chavez (1988) and Song and others (2001).

All analytical processing described herein was carried out in one pass, producing the output file provided with this map (map sheet). This processing takes 2 minutes, 53 seconds per full Landsat 8 OLI scene on an Intel Core i7 Gulftown processor running at 3.7 gigahertz (GHz), including the computation of reduced-resolution pyramid layers for fast display. This rapid processing allows the algorithm to be easily and cost effectively applied to large quantities of scenes in order to map large areas. It also permits the processing of multiple scenes acquired on different dates to ensure optimal output map quality when classification issues related to dry vegetation cover, soil moisture content, and (or) adverse atmospheric conditions are encountered in a scene.

Mineral Group and Green Vegetation Indices

Six ratio-based spectral indices were generated. They highlight specific mineral groups by exploiting diagnostic absorption feature characteristics derived from published spectral libraries. Five of these indices are identical to those used for the automated analysis of Landsat 7 ETM+ data described by Rockwell (2013a). Table 3 shows the Landsat 8 and equivalent Landsat 7 spectral indices using band numbers of the respective sensors because the band number designations have changed from Landsat 7 to Landsat 8 (table 2). For example, the five Landsat 7 equivalent band indices are shown beneath those of Landsat 8 for clarity. The new index used for iron sulfate mineral species differentiation is described below.

Iron Sulfate Mineral Index

Reflectance spectra of jarosite and most other iron sulfate minerals show strong absorption at the Landsat 8 OLI "coastal aerosol" band 1 (0.43–0.45µm, table 2) relative to band 2 (0.45–0.51µm). This in contrast to iron oxide and hydroxide minerals such as hematite and goethite, which show generally flat spectral shapes in this wavelength region (Crowley and others, 2003; Clark and others, 2007) (fig. 1). Notably, Landsat 7 ETM+ lacks this new and critical coastal aerosol band (table 2). A Landsat 8 OLI 2/1 ratio was used to highlight areas characterized by a spectral shape with a strong positive reflectance slope between bands 1 and 2. Similar to the Landsat 7 ETM+ 4/3 ratio described by Rockwell (2013a) (table 3), the Landsat 8 OLI 5/4 ratio highlights areas of deep absorption in band 4 (red wavelengths) relative to band 5 (near-infrared wavelengths), which typically include areas of dense, green vegetation with abundant chlorophyll. Areal spectral mixtures of iron-bearing soils and green vegetative

Table 3. Material indices used for analysis of Landsat 7 and Landsat 8 data, showing respective band designations for the two sensors.

[Rockwell (2013a) describes the prior five Landsat 7 ETM+ indices and their utilities in greater detail]

Material Index name	Landsat 7 ETM+Material Index (Rockwell, 2013a)	Landsat 8 OLI Material Index
Ferric iron 1 "redness"	3 / 1	4 / 2
Ferric iron 2	3 / 1 × (3 + 5) / 4	4 / 2 × (4 + 6) / 5
Ferrous iron, coarse-grained ferric iron, and fire ash	(2 + 5) / (3 + 4)	(3 + 6) / (4 + 5)
Clay, sulfate, mica, and marble	5 / 7 − 4 / 3	6 / 7 − 5 / 4
Green vegetation	4 / 3	5 / 4

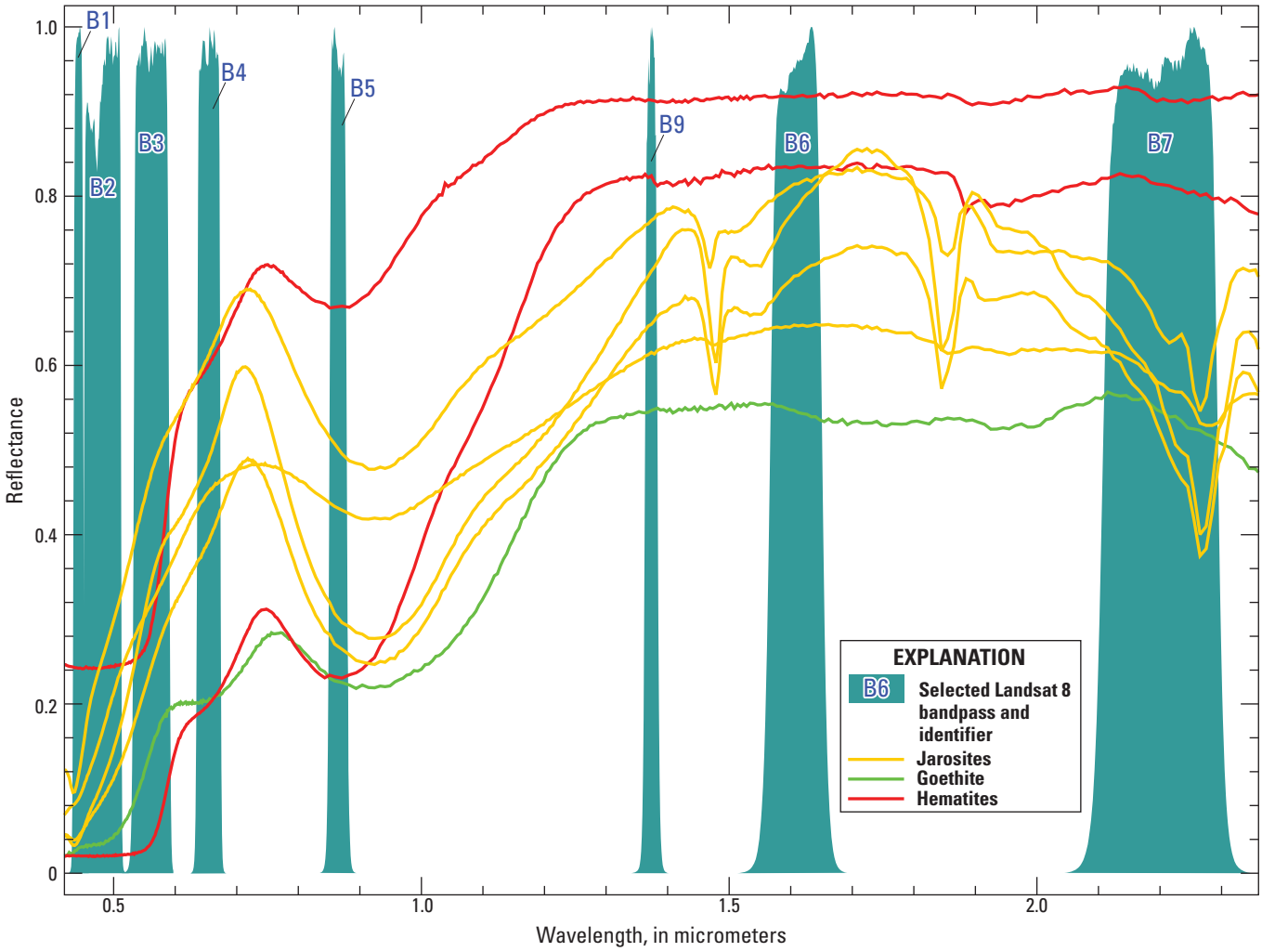

Figure 1. Reflectance spectra of ferric iron minerals showing the visible (VIS), near-infrared (NIR), and shortwave-infrared (SWIR) regions (from Clark and others, 2007). Jarosites are shown in orange-yellow, goethite in green, and hematites in red. Numbered bandpasses of the Landsat 8 OLI bands are shown in blue (for example, B1 is the band 1 bandpass). Note deep absorption in Landsat band 1 (B1) relative to band 2 (B2) for jarosites that is not present for goethite and hematite. Also note the deep and wide absorption feature near band 5 (B5, approximately 0.9 micrometers [μm]) caused by crystal field electronic transitions. This feature is typically deeper for jarosite than for goethite and hematite but is highly dependent on mineral grain size (Clarke, 1999). Jarosite will always show some vibrational absorption at band 7 (B7), whether it is attributed to the iron hydroxide (Fe-OH) feature (shown), or an aluminum hydroxide (Al-OH) feature caused by phyllosilicates (for example, clays and micas) and (or) sulfate (for example, alunite) minerals that occur in the same rock, especially on weathered pyritic rock where supergene clay minerals are common (Rockwell and others, 2005). Ground surfaces with goethite and hematite will not necessarily have this feature.

regrowth or young agricultural crops have a strong reflectance peak in the green wavelengths relative to the ultraviolet (UV), ultra-blue, blue, and red wavelength regions, resulting in relatively high 2/1 ratio values. The iron sulfate mineral index, 2/1–5/4, was generated by subtracting the results of the 5/4 ratio from results of the 2/1 ratio to focus the index results on surfaces free of green vegetation. Figure 2 shows the iron mineral spectra from figure 1 convolved to Landsat 8 OLI spectral resolution. The important differences in spectral shape between bands 1 and 2 for the two groups of minerals exploited by the iron sulfate index are clearly seen even at the relatively low spectral resolution of the Landsat 8 OLI sensor.

Image Processing for Masking and Index Thresholding

Dark Area Masking

Landsat ratio results can be spurious in areas of low surface albedo, including those with poor solar illumination caused by terrain shadow (Knepper, 2010). Such areas were masked from analysis using thresholds of Landsat 8 OLI band 6 determined through examination of many scenes from different climates, land cover, and terrain relief. Any pixel with a raw band 6 DN value less than 15,000 (12-bit) is removed from all index results other than the green vegetation index.

Water Masking

Water and snow are characterized by intense absorption in the SWIR relative to the visible spectral region and may cause spurious mineral group classifications. A Landsat 8 OLI 1/6 ratio is used to highlight this spectral characteristic of water-bearing volatiles, which have a steep decrease in reflectance between the ultra-blue and SWIR wavelength regions. A threshold value for the ratio was chosen based on examination of standing water and snow in many Landsat scenes. A mask was created by applying the threshold to the 1/6 ratio result. The mask was then applied to index results other than the green vegetation index to remove data from areas of snow and standing water. Turbid water, shallow water with a bright substrate, and mixtures of thin or melting snow and vegetation (including around the edges of glaciers and alpine snow fields) have reduced absorption in the SWIR and may not have been entirely removed by this masking process.

Final Index Thresholding and Clipping

Similar to what was done for the Landsat 7 ETM+ spectral indices (Rockwell, 2013a), the final Landsat 8 OLI indices were created by isolating the highest values using a common standard deviation threshold, followed by carrying out an index-specific clip (removal) of the lowest index values. The threshold for this clipping was based on extensive testing of scenes from a variety of climates, underlying bedrock and surficial geology, terrain relief, and alteration types. These clips are minor in scope and were determined based on detailed comparisons of the index results to mineral maps created from spectroscopic analysis of ASTER and AVIRIS imagery over known, hydrothermally altered rocks and mining districts and mill sites with abundant mine waste and tailings deposits (see Regional Studies section in viewer from Rockwell and others, 2015). The low-end index values that are removed, in order of decreasing number of values removed, represent (1) potential iron sulfate minerals, (2) ferrous iron, oxidized basalt, fire ash, and clay-sulfate-mica-marble, (3) minor and major ferric iron, and (4) green vegetation. The relatively high degree of clipping of the first two indices is caused by the spectral similarity of these mineral groups to other surface features at Landsat spectral resolution. A lower degree of confidence in the accuracies of results for these two groups is necessitated. Increased clipping of low-end values will result in fewer detected pixels in an index and increased confidence in the accurate classification of those that remain. However, interpreted occurrences of a particular mineral group in lower abundance will be removed, which has the effect that most mapped mineral groups will be those on rock outcrops and adjacent, proximal alluvium rather than distal alluvium derived from those outcrops.

The bandpass (or full width half maximum, FWHM) of Landsat 8 OLI band 7 (table 2) is significantly narrower than that of the comparable Landsat 7 ETM+ band (USGS, 2013). This fact makes it less likely with Landsat 8 data than was the case with Landsat 7 data that carbonates and other minerals with strong absorptions between 2.30 and 2.34 μm (for example, chlorite, epidote, serpentine, talc, hectorite, and saponite) will be detected using the clay-sulfate-mica-marble index. Therefore, the clay-sulfate-mica-marble index based on Landsat 8 OLI data will be less affected by spectral mixing and will more accurately identify surfaces spectrally dominated by Al-OH phyllosilicates and (or) sulfates. The clipping value for the clay-sulfate-mica-marble index was determined based on known occurrences of exposed clay, sulfate, and mica minerals, but not carbonates and other minerals with SWIR absorptions in the 2.3 μm region. Nevertheless, some exposures with very abundant carbonate minerals, including marbles, particularly those with a dolomitic component, are identified by the clay-sulfate-mica-marble index. Dolomite is more likely to be detected by a 6/7 ratio than is calcite because it is characterized by a carbonate-related absorption centered near 2.32 μm with a short-wavelength shoulder that extends into the wavelength region measured by Landsat 8 OLI band 7. The Landsat 8-derived mapping results are more likely to identify mineral groups on surfaces with acid-producing potential, since surfaces with carbonate and chlorite that have acid-neutralizing potential are less likely to be identified.

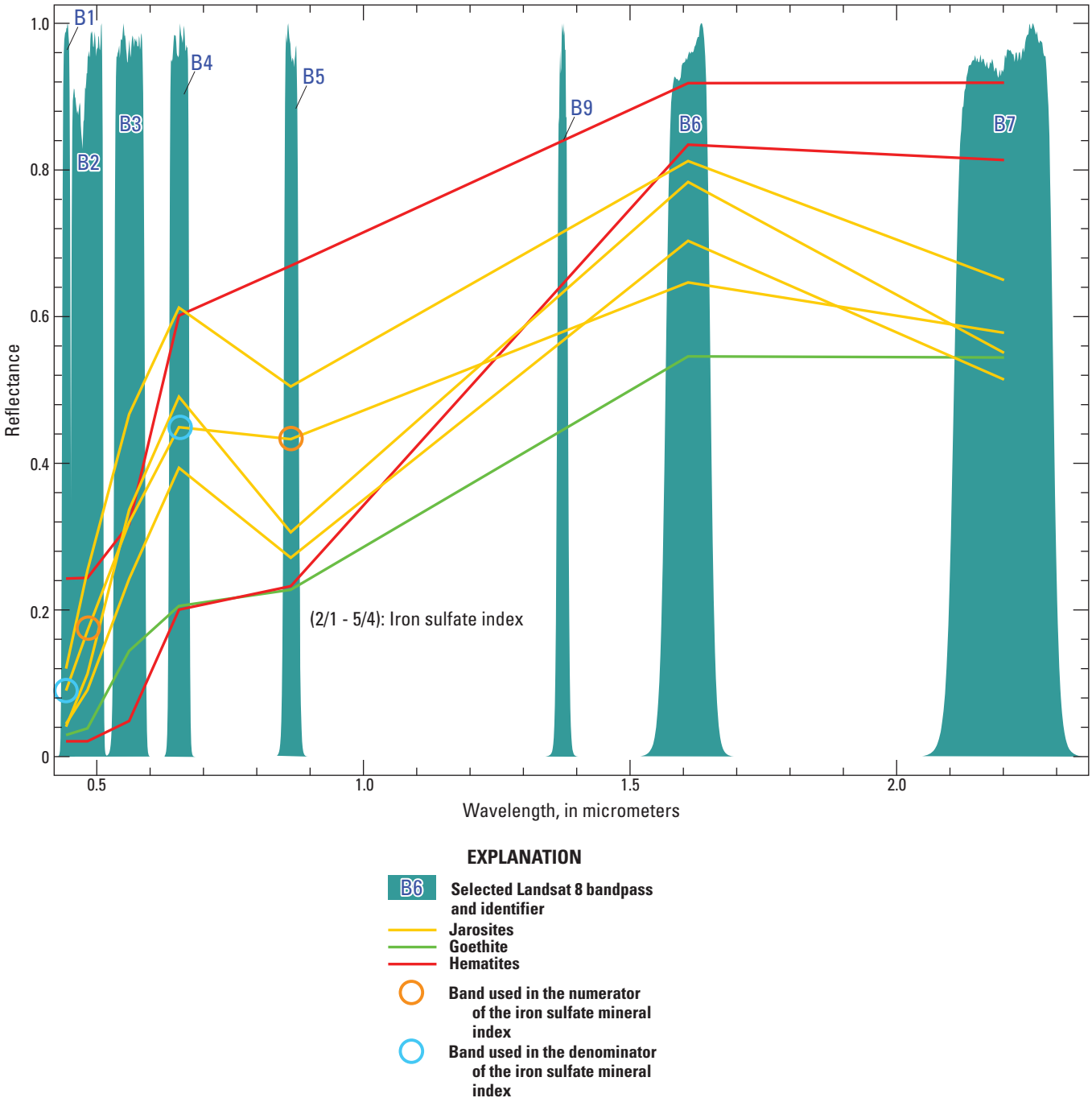

Figure 2. Plot of ferric iron mineral spectra from figure 1 convolved to Landsat 8 OLI spectral resolution. Jarosites are shown in orange-yellow, goethite in green, and hematites in red. Numbered bandpasses of the Landsat 8 OLI bands are shown in blue. Orange circles show bands used in the numerator of the iron sulfate mineral index, and light blue circles show bands used in the denominator.

Modeling of Mineral Groups through Boolean Combination of Index Results

For the purposes of combining the six indices into a more easily visualized single map and assigning GIS-ready descriptive attributes to each pixel, Boolean algebra was used to examine instances where pixels were assigned to one or more indices. Table 4 shows the logic of each algebraic expression. To account for various combinations of index co-occurrence in a pixel, 18 output classes of mineral groups and green vegetation were developed (see map sheet). A nineteenth class (no. 15) indicating areas with no data was added manually after the analysis was completed, when necessary. For example, class 15 was assigned to areas where the land surface is obscured by smoke, clouds, cloud shadow, and (or) corrupted Landsat pixels. An example of this 'no data' class can be seen in the northeastern part of the Landsat scene covering the western San Juan Mountains used in this study (see map sheet), which was partially obscured by smoke from a forest fire that was active on the date of scene acquisition. Figure 3 shows the color-coded explanation of the exposed surface mineral maps generated by the analysis algorithm.

Classes 9, 12, 14, and 17–19 were designed to indicate the potential presence of iron sulfate minerals with possible NAP. Classes relating to iron sulfate minerals and NAP were first determined from analysis of imaging spectrometer data of known exposures of weathered pyrite, jarosite, goethite, and mixtures thereof that were confirmed by field verification and sampling surveys (Swayze and others, 2000; Dalton and others, 2005, 2007; Rockwell and others, 2005, 2015; Rockwell, 2012). These classes were developed to delineate the zonation of iron-bearing minerals surrounding and (or) down gradient from sources of pyrite. For a pixel to be classified as one of these classes, it must contain non-zero values of both the iron sulfate and clay-sulfate-mica-marble indices (fig. 1). The Boolean operators for these classes include and exclude various index values to account for observed spectral variations in iron sulfide-, iron sulfate- and iron hydroxide-bearing rocks, mine waste, and mill tailings. Spectral variations dependent on mineral abundance and grain sizes, resulting from charge transfers and crystal field electronic transition absorptions between 0.45 and 0.9 μm, are of particular importance for NAP.

The more indices required for a class (as indicated by AND operators in table 4), the more restrictive the logic, which reduces the likelihood of a class being identified in a particular Landsat 8 scene. Class 14 is the iron sulfate mineral class with the least restrictive logic, as it must include only the iron sulfate and clay-sulfate-mica-marble indices. This class was identified in the highly pyritic core zone of tailings at the Bauer Mill near Stockton, Utah. AVIRIS-based mapping identified weathered pyrite in the same area (Rockwell and others, 2005, 2015). Class 14 was also identified in waste rock and tailings of the Goldfield mining district, Nevada, in which pyrite, jarosite, and (or) copiapite were identified using AVIRIS-based mapping with supporting fieldwork (Rockwell, 2012; Rockwell and others, 2015). Weathered and fresh pyrite is characterized by strong charge transfer absorption in the UV (Clark and others, 2007), making detection by the iron sulfate mineral index likely. However, only weak absorption near 0.9 μm suggests that pyrite should not be detected by the ferric iron index 2 (table 3) that identifies absorptions in this wavelength region (Landsat 8 OLI band 5). For this reason, the ferric iron 2 index was not selected as a required index for classification of class 14. Since the absorptions required to be present match those of weathered pyrite and because the class was identified in highly pyritic areas, the class was assigned the highest estimated relative NAP value (table 4), and the description "clay, sulfate, mica, and/or marble with possible oxidizing sulfides and minor iron sulfate" was assigned to its Class Name.

Class 14 was also identified in several large playa lakes in northern Nevada, including those in northern Grass Valley, Edwards Creek Valley, Diamond Valley, Newark Lake in Newark Valley, Big Smoky Valley, and in central Railroad Valley (Rockwell and others, 2015). Figure 4 shows a laboratory reflectance spectrum of a sample of the playa surface from northern Grass Valley. Deep charge transfer absorption is present in the shortest visible wavelengths (0.4 μm). Ferric and (or) ferrous iron absorptions is present near 1.0 μm. Hydroxyl-related absorption is present in the SWIR near 2.2 and 2.31 μm. X-ray powder diffraction (XRD) analyses of the sample identified the minerals muscovite 2M (56 percent), analcime (17 percent), calcite (14 percent), quartz (7 percent), halite (5 percent), and albite (trace). The sample contains abundant iron (45,200 ppm Fe) (table 5), but no iron-bearing minerals were detected using XRD. These results suggest that the deep UV absorption in the spectrum is caused by amorphous iron in the playa surface and will result in detection by the iron sulfate index. Based on these results, the description "amorphous iron in playa surfaces and other high-albedo soils" was appended to the name of class 14. The non-restrictive logic of class 14 necessitates careful interpretation of this class where identified, and the local geologic and anthropogenic environment must be considered. Oxidizing pyrite (and much less commonly other sulfides) should be expected mainly when class 14 is identified within altered volcanic rocks, mine waste, or mill tailings. Amorphous iron in most soils or playa lake sediments is not typically associated with increased NAP.

Table 4. Boolean logic used to combine Landsat 8 ratio-based index results into the single, classified map shown on map sheet.

[Cells with dashes represent NOT operators. AND/NOT indicates AND or NOT operators. X, single index used to generate output class. The first column indicates both the designated number (#) of the output mineral or vegetation group class and the digital number (DN) of that class in the GIS-ready image file provided in the data release for this report (L8_P35R34_SilvertonCO.img, Rockwell and Gnesda, 2021). For comparison purposes, the indices from Landsat 8 are shaded red and indices from Landsat 7 (L7) are within brackets and shaded blue. Pixel assignment to an output class is carried out in order from top of table downwards, with the pixel being assigned to the first class for which all conditions are met; NAP, estimated relative degree of net acid production (or acid-producing potential) based on comparison with AVIRIS-derived maps (Rockwell and others, 2005, 2015) of iron-bearing minerals in highly pyritic areas and relative NAP values of various common iron-bearing minerals (Swayze and others, 2000), where 1=high and 5=low among classes with detected iron sulfate minerals]

Output Class # and DN Value	Class Color	Class Name (Materialid attribute)	Material Indices						NAP
			Iron sulfate mineral index 2/1 – 5/4 [no L7 equiv.]	Ferric iron 1 "redness index" 4/2 [3/1]	Ferric iron index 2 4 / 2 × (4 + 6) / 5 [3 / 1 × (3 + 5) / 4]	Ferrous iron, coarse-grained ferric iron, and fire ash index (3 + 6) / (4 + 5) [(2 + 5) / (3 + 4)]	Clay, sulfate, mica, and marble index 6 / 7 – 5 / 4 [5 / 7 – 4 / 3]	Green vegetation index 5 / 4 [4 /3]	
1	Light brown	Minor ferric iron (high redness, often includes hematite)	—	X	—	—	—	—	—
2	Light magenta	Major ferric iron	AND/OR	AND	AND/OR	—	—	—	—
3	Purple	Ferric +/- ferrous iron	AND/OR	AND/OR	AND/OR	AND	—	—	—
4	Dark cyan	Ferrous or coarse-grained ferric iron (may include oxidized basalts, fire ash, some moist soils, and any blue/green rocks)	—	—	—	X	—	—	—
5	Green	Clay, sulfate, mica, and (or) marble	—	—	—	—	X	—	—
6	Yellow	Clay, sulfate, mica, and (or) marble + minor ferric iron	—	AND	—	—	AND	—	—
7	Orange	Clay, sulfate, mica, and (or) marble + moderate to major ferric iron	—	—	AND	AND/NOT	AND	—	—

Table 4. Boolean logic used to combine Landsat 8 ratio-based index results into the single, classified map shown on map sheet.—Continued

[Cells with dashes represent NOT operators. AND/NOT indicates AND or NOT operators. X, single index used to generate output class. The first column indicates both the designated number (#) of the output mineral or vegetation group class and the digital number (DN) of that class in the GIS-ready image file provided in the data release for this report (L8_P35R34_SilvertonCO.img, Rockwell and Gnesda, 2021). For comparison purposes, the indices from Landsat 8 are shaded red and indices from Landsat 7 (L7) are within brackets and shaded blue. Pixel assignment to an output class is carried out in order from top of table downwards, with the pixel being assigned to the first class for which all conditions are met; NAP, estimated relative degree of net acid production (or acid-producing potential) based on comparison with AVIRIS-derived maps (Rockwell and others, 2005, 2015) of iron-bearing minerals in highly pyritic areas and relative NAP values of various common iron-bearing minerals (Swayze and others, 2000), where 1=high and 5=low among classes with detected iron sulfate minerals]

Output Class # and DN Value	Class Color	Class Name (Materialid attribute)	Material Indices						
			Iron sulfate mineral index 2/1 – 5/4 [no L7 equiv.]	Ferric iron 1 "redness index" 4/2 [3/1]	Ferric iron index 2 4 / 2 × (4 + 6) / 5 [3 / 1 × (3 + 5) / 4]	Ferrous iron, coarse-grained ferric iron, and fire ash index (3 + 6) / (4 + 5) [(2 + 5) / (3 + 4)]	Clay, sulfate, mica, and marble index 6 / 7 – 5 / 4 [5 / 7 – 4 / 3]	Green vegetation index 5 / 4 [4 /3]	NAP
8	Reddish orange	Clay, sulfate, mica, and (or) marble + major ferric iron	—	AND	AND	AND/NOT	AND	—	—
9	Hot pinkish red	Clay, sulfate, mica, and/or marble + major ferric iron with possible iron sulfate and hydroxide (commonly in argillically-altered rocks)	AND	AND	AND	AND	AND	—	5
10	Cyan	Clay, sulfate, mica, and/or marble + ferrous or coarse-grained ferric iron	—	AND/NOT	—	AND	AND	—	—
11	Dark green	Dense, green vegetation	—	—	—	—	—	AND	—
12	Red	Clay, sulfate, mica, and/or marble + major ferric iron with possible oxidizing sulfides and major iron sulfate	AND	AND	—	—	AND	—	2

Table 4. Boolean logic used to combine Landsat 8 ratio-based index results into the single, classified map shown on map sheet.—Continued

[Cells with dashes represent NOT operators. AND/NOT indicates AND or NOT operators. X, single index used to generate output class. The first column indicates both the designated number (#) of the output mineral or vegetation group class and the digital number (DN) of that class in the GIS-ready image file provided in the data release for this report (L8_P35R34_SilvertonCO.img, Rockwell and Gnesda, 2021). For comparison purposes, the indices from Landsat 8 are shaded red and indices from Landsat 7 (L7) are within brackets and shaded blue. Pixel assignment to an output class is carried out in order from top of table downwards, with the pixel being assigned to the first class for which all conditions are met; NAP, estimated relative degree of net acid production (or acid-producing potential) based on comparison with AVIRIS-derived maps (Rockwell and others, 2005, 2015) of iron-bearing minerals in highly pyritic areas and relative NAP values of various common iron-bearing minerals (Swayze and others, 2000), where 1=high and 5=low among classes with detected iron sulfate minerals]

Output Class # and DN Value	Class Color	Class Name (Materialid attribute)	Material Indices						NAP
			Iron sulfate mineral index 2/1 – 5/4 [no L7 equiv.]	Ferric iron 1 "redness index" 4/2 [3/1]	Ferric iron index 2 4 / 2 × (4 + 6) / 5 [3 / 1 × (3 + 5) / 4]	Ferrous iron, coarse-grained ferric iron, and fire ash index (3 + 6) / (4 + 5) [(2 + 5) / (3 + 4)]	Clay, sulfate, mica, and marble index 6 / 7 – 5 / 4 [5 / 7 – 4 / 3]	Green vegetation index 5 / 4 [4 /3]	
13	Olive green	Sparse, green vegetation + ferric iron	AND/NOT	AND	AND/NOT	—	—	AND	—
14	Pale red (salmon)	Clay, sulfate, mica, and/or marble with possible oxidizing sulfides and minor iron sulfate, or amorphous iron in playa surfaces and other high-albedo soils	AND	—	—	—	AND	—	1
17	Medium red	Clay, sulfate, mica, and/or marble + major ferric iron with possible major iron sulfate and hydroxide (commonly proximal zones of weathered, highly pyritic rocks and mine waste)	AND	AND	AND	—	AND	—	3

Table 4. Boolean logic used to combine Landsat 8 ratio-based index results into the single, classified map shown on map sheet.—Continued

[Cells with dashes represent NOT operators. AND/NOT indicates AND or NOT operators. X, single index used to generate output class. The first column indicates both the designated number (#) of the output mineral or vegetation group class and the digital number (DN) of that class in the GIS-ready image file provided in the data release for this report (L8_P35R34_SilvertonCO.img, Rockwell and Gnesda, 2021). For comparison purposes, the indices from Landsat 8 are shaded red and indices from Landsat 7 (L7) are within brackets and shaded blue. Pixel assignment to an output class is carried out in order from top of table downwards, with the pixel being assigned to the first class for which all conditions are met; NAP, estimated relative degree of net acid production (or acid-producing potential) based on comparison with AVIRIS-derived maps (Rockwell and others, 2005, 2015) of iron-bearing minerals in highly pyritic areas and relative NAP values of various common iron-bearing minerals (Swayze and others, 2000), where 1=high and 5=low among classes with detected iron sulfate minerals]

Output Class # and DN Value	Class Color	Class Name (Materialid attribute)	Material Indices						NAP
			Iron sulfate mineral index 2/1 – 5/4 [no L7 equiv.]	Ferric iron 1 "redness index" 4/2 [3/1]	Ferric iron index 2 4 / 2 × (4 + 6) / 5 [3 / 1 × (3 + 5) / 4]	Ferrous iron, coarse-grained ferric iron, and fire ash index (3 + 6) / (4 + 5) [(2 + 5) / (3 + 4)]	Clay, sulfate, mica, and marble index 6 / 7 – 5 / 4 [5 / 7 – 4 / 3]	Green vegetation index 5 / 4 [4 /3]	
18	Dark red	Clay, sulfate, mica, and/or marble + major ferric iron with possible moderate to major iron sulfate and hydroxide (commonly distal zones of weathered, highly pyritic rocks and mine waste)	AND	AND/NOT	AND	AND/NOT	AND	—	4
19	Reddish purple	Clay, sulfate, mica, and/or marble + ferrous or coarse-grained ferric iron with possible minor iron sulfate	AND	AND/NOT	—	AND	AND	—	6

Figure 3. Color-coded explanation of analysis results produced by the algorithm presented herein. This information is also available in the Explanation on the map sheet, within the provided ERDAS Imagine raster image (see data release, Rockwell and Gnesda, 2021), and associated metadata. The classes are ordered with respect to relative estimated NAP or acid-producing potential from top (high) to bottom (low).

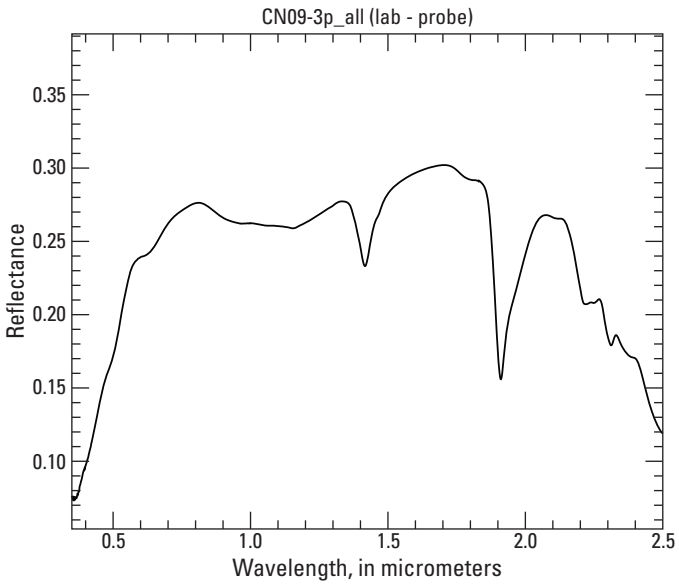

Figure 4. Laboratory reflectance spectrum of a sample of playa surface from northern Grass Valley, Lander County, Nevada. Sample was collected approximately 14 kilometers south of Cortez, Nevada. The absorption feature near 2.31 micrometers (μm) is most likely caused by lithium-bearing (table 4) hectorite in the sample, although this mineral was not detected by X-ray powder diffraction analyses of bulk sample and clay separates.

The deep absorption in the UV and short VIS wavelengths (including Landsat 8 OLI band 1) caused by amorphous ferric iron minerals may also cause detection of the iron sulfate mineral classes, particularly class 14, on other high-albedo soils, including those in fallow agricultural fields. Sparse, green vegetation in fallow fields can be spectrally characterized by weak chlorophyll absorption in Landsat 8 band 4 (preventing classification as green vegetation, class 11) and increased reflectance in the green wavelengths (band 3). These spectral features of vegetation can be mixed with those of exposed soils in the fields, which have significant absorption in Landsat 8 bands 1 and 2 related to amorphous or crystalline ferric iron and absorption in band 7 related to clay or mica minerals. The combined spectral characteristics of this type of areal mixture can result in classification as one or more of the iron sulfate mineral classes, especially in Landsat scenes where no iron sulfate minerals are actually present. In such scenes, the mixed spectral features present in some fallow fields show the highest values for the iron sulfate mineral index (table 3) compared to those of other surfaces present in the scene, whereas actual iron sulfate minerals would have significantly higher values for this index. Such classification issues represent a drawback to any ratio-based analysis technique for which hard-coded detection thresholds of index results are not applied. Iron sulfate mineral groups identified in agricultural areas are manually assigned new class designations to account for erroneous classification.

Classes 12 and 17 were designed to identify areas with the most abundant iron sulfate minerals. These classes typically occur in areas proximal to zones of weathered, highly pyritic rocks, in some places surrounding or adjacent to occurrences of class 14 in which jarosite and other iron sulfate minerals are only weakly developed on sulfide-bearing rock. Like class 14, class 12 does not require deep crystal field absorption near 0.9 μm (ferric iron 2 index) to be identified, so some pyritic surfaces with only partially developed jarosite will be erroneously included in class 12 designations. Deep charge transfer absorption in the UV (ferric iron index 1) is required for a pixel to be classified as class 12 or 17, meaning that surfaces with strong red, orange, and yellow color are likely to be included. Class 17 additionally requires deep crystal field absorption (ferric iron 2 index) to be identified. As this absorption can be deep and wide for both iron sulfates and hydroxides, minerals of both of these ferric iron species are likely to be classified as class 17.

The iron sulfate mineral class with the most restrictive logic is class 9, which requires non-zero values in all indices except for the green vegetation index. Class 9 typically occurs in undisturbed, intensely altered rocks bearing abundant jarosite, most commonly in zones of pyrite-bearing advanced argillic alteration. An example occurrence of this class is located east of Diamond (peak) in the Goldfield mining district, Nevada (fig. 5).

The other output classes described in table 4 are self-explanatory, and the classes not including information from the iron sulfate mineral index are identical to the output classes of the Landsat 7 data analysis methodology described by Rockwell (2013a).

Discussion of Regional-Scale Mapped Mineral Zonation Patterns

The exposed surface mineral maps and vegetation generated by the Landsat 8 OLI data analysis methodology presented here provide substantial increases in identification and differentiation of exposed surface mineral groups compared to the maps generated from Landsat 7 ETM+ data (Rockwell, 2013a), particularly for iron-bearing mineral groups. Figure 5 compares the new Landsat 8-derived mapping results with the Landsat 7-derived results of Rockwell and others (2015). While both map products identify similar areas as clay-sulfate-mica-marble ± ferric iron, the Landsat 8-derived map depicts these areas in more detail, allowing for more accurate delineation of zonation related to iron mineral occurrence. Importantly, the Landsat 8-derived map may also be used to identify areas with potential iron sulfate minerals that are more likely to contain pyrite in greater abundance. The Landsat 8-derived map allows a user to more rapidly focus on smaller areas when attempting to identify more pyritic zones in hydrothermally altered rocks, mine waste, or mill tailings.

Table 5. Inductively coupled plasma mass spectrometry (ICP-MS) acid digestion results for a sample of playa surface from northern Grass Valley, Nevada.

[Modified from Briggs and Meier (2002). Note measured 457 parts per million (ppm) lithium in the sample. Lithium (208 ppm average) was also detected from a 140-centimeter auger hole in these playa sediments by Bohannon and Meier (1976). Antimony (Sb) was not available (Na). Reflectance spectrum of sample is shown in figure 4. Sample location (WGS84 datum): 116.60307°W, 40.04559°N]

Element	ICPMS ACID result (ppm)
Ag	<1
Al	80000
As	63.4
Ba	624
Be	2.6
Bi	0.44
Ca	47800
Cd	0.65
Ce	53.4
Co	15.6
Cr	56.1
Cs	31.7
Cu	53.8
Fe	45200
Ga	17
K	41700
La	27.4
Li	457
Mg	45700
Mn	925
Mo	5.1
Na	57800
Nb	21
Ni	36.5
P	1160
Pb	20.6
Rb	140
Sb	Na
Sc	13.4
Sr	495
Th	13.3
Ti	3260
Tl	0.92
U	3.66
V	170
Y	18.7
Zn	154

To validate the results of the automated analysis methodology, derived mineral group maps of several well-known mineralized and (or) hydrothermally altered areas in the western United States are presented below and are compared with field-verified maps generated from detailed spectroscopic analysis of AVIRIS and (or) ASTER data (Rockwell, 2012). These maps are subsets of a seamless mineral group map of the southwestern U.S. (Rockwell, 2013b; Rockwell and others, 2015).

Most hydrothermal alteration and polymetallic mineral deposits in the Silverton and Lake City regions of the western San Juan Mountains, Colorado (map sheet), formed in high-sulfidation, magmatic-hydrothermal environments, and thus typically contain abundant pyrite that weathers to ferric iron minerals, including jarosite. Within the volcanic rocks of the Silverton caldera region, most areas of advanced argillic, argillic, and phyllic alteration containing ferric iron minerals (Bove and others, 2007; Rockwell, 2012) have been identified as class 8 surrounded by concentric zones with weaker ferric iron concentrations, classified as class 6 (table 4). Commonly, these altered zones comprising classes 8 and 6 are surrounded by or adjacent to broader areas of clay or mica minerals classified as class 5, which are generally devoid of ferric iron minerals. These outer areas of class 5 correspond generally to weakly argillized and (or) propylitized rocks containing sericite ± minor clay minerals.

Along incised stream gullies on the southeast wall of Chicago Basin, below Columbine Pass in the Needle Mountains, Landsat 8 OLI mapped class 8 surrounded by class 6, grading outward to class 5. Several pixels classified as iron sulfate minerals—classes 12, 14, 17, and 19—were mapped immediately to the east. Similarly, sericitic alteration with ferric iron, possibly of the phyllic variety, was mapped using ASTER data (Rockwell, 2012). This alteration was identified as clay-sulfate-mica-marble + ferric iron in an analysis of Landsat 7 data analysis (Rockwell, 2013a). The alteration directly overlies and is genetically related to the late Miocene Chicago Basin stock (unit Tui, map sheet). Schmitt and Raymond (1977) described this alteration as phyllic (quartz-sericite-pyrite or quartz-sericite-kaolinite-pyrite) with local pyrophyllite and identified porphyry-type molybdenum mineralization associated with the stock.

Many occurrences of the iron sulfate mineral classes (table 4) were mapped in the western San Juan Mountains using the Landsat 8 OLI data. Occurrences of jarosite + sericite on Rolling Mountain 15 km west-southwest of the town of Silverton, identified using AVIRIS (Dalton and others, 2005) and ASTER (Rockwell, 2012) data, were mapped as output class 17 (map sheet). Other jarositic rocks mapped using ASTER data were identified as class 14 on Sliderock Ridge 4.5 km west-southwest of Rolling Mountain. Other important occurrences of iron sulfate minerals identified using the Landsat 8 data and corroborated with AVIRIS data include the following:

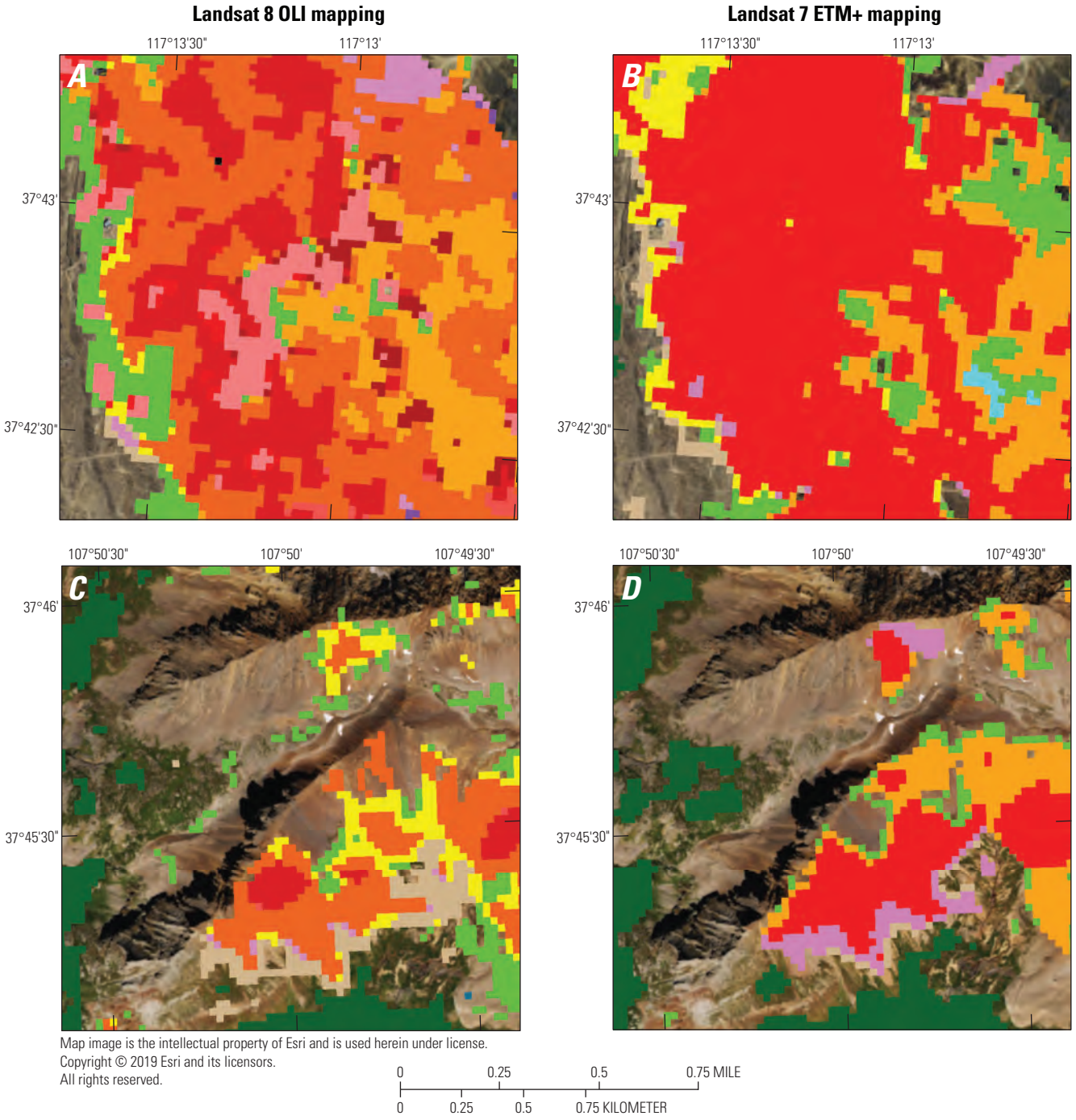

Figure 5. Comparison of map products generated by Landsat 8 data analysis (shown on left) and Landsat 7 data analysis (shown on right): *A*. Landsat 8-derived map of main mining area of Goldfield district, Nevada, centered on the Florence Mine. Refer to figure 3 for map explanation. Note highly pyritic mine waste and altered rock identified as class 14 grading outwards into highly jarositic areas identified as classes 12 and 17. Area is also shown in figure 6. *B*. Landsat 7-derived map (Rockwell, 2013a) of same area. Mine waste and altered rock classified as clay-sulfate-mica-marble mineral group (in this case primarily clay minerals and some alunite) + major ferric iron are shown in red. Orange indicates clay-sulfate-mica-marble + moderate to major ferric iron, yellow indicates clay-sulfate-mica-marble + minor ferric iron, and green indicates clay-sulfate-mica-marble with no ferric iron detected. *C*. Landsat 8-derived map of jarositic rocks in the Rolling Mountain area, San Juan Mountains, Colorado (see map sheet). Refer to figure 3 for map explanation. *D*. Landsat 7-derived map (Rockwell, 2013a) of Rolling Mountain area. Scale 1:25,000.

Figure 5. Comparison of map products generated by Landsat 8 data analysis (shown on left) and Landsat 7 data analysis (shown on right): *A*. Landsat 8-derived map of main mining area of Goldfield district, Nevada, centered on the Florence Mine. Refer to figure 3 for map explanation. Note highly pyritic mine waste and altered rock identified as class 14 grading outwards into highly jarositic areas identified as classes 12 and 17. Area is also shown in figure 6. *B*. Landsat 7-derived map (Rockwell, 2013a) of same area. Mine waste and altered rock classified as clay-sulfate-mica-marble mineral group (in this case primarily clay minerals and some alunite) + major ferric iron are shown in red. Orange indicates clay-sulfate-mica-marble + moderate to major ferric iron, yellow indicates clay-sulfate-mica-marble + minor ferric iron, and green indicates clay-sulfate-mica-marble with no ferric iron detected. *C*. Landsat 8-derived map of jarositic rocks in the Rolling Mountain area, San Juan Mountains, Colorado (see map sheet). Refer to figure 3 for map explanation. *D*. Landsat 7-derived map (Rockwell, 2013a) of Rolling Mountain area. Scale 1:25,000.—Continued

- the tailings deposits bearing smectite and pyrite from the Pride of the West Mill near Howardsville (map sheet) 7 km northeast of Silverton;
- phyllic alteration along Ohio Gulch 5.3 km north-northwest of Silverton;
- highly pyritic mine waste along the North Fork of Cement Creek below the Upper Gold King Mine just northeast of Gladstone (map sheet) 9.6 km north-northeast of Silverton;
- phyllic-altered areas of Red Mountains No. 1, No. 2, and No. 3 3 km west and northwest of Gladstone;
- phyllic alteration just south of the Big Colorado Mine along the South Fork of Cement Creek 2 km south of Gladstone; and
- phyllic alteration on California Mountain 5 km northeast of Gladstone.

Several pixels classified as class 9 are located within highly pyritic, primarily phyllic-altered rocks overlying molybdenum-copper porphyry mineralization on "Mount Moly" (3,792-meter elevation) 7.5 km west-northwest of the town of Silverton. Class 9 was mapped on surfaces in which jarosite + sericite ± kaolinite was identified using AVIRIS data analysis (Dalton and others, 2005). The jarosite is so abundant that it was detected in both the VNIR and SWIR spectral regions of the AVIRIS data. The AVIRIS data analysis and field mapping (Ringrose, 1982; Bove and others, 2007) identified pyrophyllite + sericite ± kaolinite ± jarosite as little as 85 m to the east, north, and southeast of some of these occurrences of class 9, providing another example of a general spatial association between class 9 and jarosite-bearing advanced argillic alteration.

Within the Silverton caldera, large zones of well-developed propylitic alteration with abundant calcite, chlorite, and epidote (Dalton and others, 2005) occur (map sheet) on steep slopes along the northwest bank of the Animas River northeast of Silverton, between Howardsville and Eureka. These propylitized volcanic rocks were identified as class 4 (ferrous iron) because of strong VNIR absorptions of chlorite and epidote. In this area, smaller zones of locally pervasive phyllic alteration (Bove and others, 2007) with more abundant sericite and ferric iron were identified as classes 8, 7, and 6 surrounded by areas of class 10 (ferrous + ferric iron, table 4). This sequence of classes indicates mineralogic zonation into the areas of more abundant chlorite and epidote and with less sericite and ferric iron. The ferrous iron mineral group was also identified within another large exposure of epidote- and calcite-bearing propylitic alteration on the western flanks of Galena Mountain east and southeast of Howardsville. These altered rocks and the similarly intense propylitic alteration northwest of Howardsville, as mentioned above, surround and locally occur within the Eocene–Miocene Sultan Mountain monzonite porphyry stock (Tmi, map sheet) that crops out just east of the Animas River and runs nearly parallel to it in this area.

Iron sulfate minerals were also identified on Red Mountain near Lake City (map sheet), with zones of class 17 surrounded by larger areas of class 9 (table 3). Alunite was identified in this area using ASTER data (Rockwell, 2012). A magmatic hydrothermal origin is suggested by the co-occurrence of class 9 (indicating abundant jarosite after pyrite within undisturbed, strongly altered rocks with abundant clay, sulfate, and [or] mica minerals) with advanced argillic alteration. Steam-heated alteration that formed close to the paleo-ground surface is commonly devoid of pyrite (Rye and others, 1992). A magmatic hydrothermal origin for the alunite deposit at Red Mountain was proposed by Bove and others (1990). Iron sulfate minerals were also identified within the highly pyritic rocks and colluvium of Slumgullion Slide 8.5 km east-northeast of Red Mountain.

Large scars from wildfires, including one in the Mesa Verde area south of Mancos, have been identified primarily as class 4 because of VNIR absorptions of ash (map sheet; Kokaly and others, 2006). Ferric iron minerals were detected across large areas in the southwestern part of the Landsat scene within Quaternary alluvium and eolian dune sands and silts (units Q, Qa, Qe, Qg, Qo, Qy, map sheet), the Cretaceous Dakota Sandstone and Cedar Mountain or Burro Canyon Formations (unit K1 in Utah), locally within the Cretaceous Cliff House Sandstone (unit Kch), and within shales and siltstones of the Jurassic Morrison Formation, Summerville Formation, and Entrada Sandstone (J1 in Utah and Jm in Colorado, New Mexico, and Arizona). Major ferric iron minerals (classes 1 and 2) were also identified in the Rock Point Formation of the Chinle Group (unit TRrp, map sheet) in northwestern New Mexico. In Arizona, ferric iron minerals were mapped within the red sandstones of the Jurassic to Triassic Glen Canyon Group (unit Jgc) and reddish sandstones and siltstones of the Jurassic San Rafael Group (unit Js). The Cretaceous Mancos Shale (units Km and Kmu, including Mesaverde Group or Formation, Frontier Sandstone, and Mowry Shale), was mapped as primarily class 5 (mica ± clay minerals with no detected ferric iron), with ferric iron (class 1) being identified mainly in the extreme south of the Landsat scene in areas where mica and clay minerals were not detected. Within these shale units, class 5 represents mainly muscovite, with gypsum and carbonate minerals possibly contributing to band 7 absorption in some localities. Classes 4 and 10 are commonly mapped within the Mancos Shale and other shale units because of the VNIR absorptions associated with the blue gray color of these rocks.

Mineral exposures related to alteration and (or) lithology were identified within quartzites, slates, and phyllites of the Proterozoic Uncompahgre Formation on Peaks One, Two, and Three and White Dome between the Grenadier Range and Elk Creek 15 km southeast of Silverton. The Landsat 8-based mapping identified mineral group 5 surrounding smaller zones of 6, 7, and 8, which correlate well with Landsat 7 ETM+

mapping of the same area (Rockwell, 2013a). Spectroscopic analysis of ASTER data (Rockwell, 2012; Rockwell and others, 2015) identified narrow, west-northwest to east-west trending zones of kaolinite ± ferric iron grading outwards to kaolinite + sericite ± ferric iron, to larger zones of sericite ± ferric iron, and finally to regional propylitic alteration containing Fe and (or) Mg sericite ± chlorite. Automated ASTER data analysis (Rockwell and others, 2015) identified these narrow zones as argillic + ferric iron (or weathered phyllic) with local adjacent argillic zones grading outwards to sericite (and [or] smectite) + ferric iron and finally to much broader zones of sericite (and [or] smectite) with local zones of ferrous iron (likely chlorite). The larger zones of sericite (identified as class 5 using Landsat 8 data) are most likely lithologic in character and represent primary or authigenic mica in the quartzite groundmass or phyllites. However, the presence of clay minerals in localized zones within the formation suggests the occurrence of fracture-controlled phyllic and (or) argillic hydrothermal alteration. The mineral mapping results in this area have not been field verified.

The Landsat 8-based mapping identified class 4 (ferrous iron) in Proterozoic felsic and hornblende gneisses, metabasalts, and metatuff (unit Xfh, map sheet) extending to the southeast from the southern flanks of Irving Peak 28 km south-southeast of Silverton. The ferrous iron-bearing minerals are possibly derived from low-grade metamorphism of volcanic rocks. ASTER-based mapping identified extensive exposures of calcite, chlorite, and possibly epidote in this area, often mixed with sericite or smectite (Rockwell, 2012; Rockwell and others, 2015). The ferrous iron mineral group (class 4) identified by the Landsat 8 mapping likely reflects the presence of chlorite, but the carbonate and Mg-OH SWIR absorptions of calcite and chlorite detected using ASTER data are too weak to be detected by the Landsat analysis, as was the case in the propylitic alteration along the Animas River northeast of Silverton discussed above. Chlorite and mixed-layer chlorite/smectite are common in low-grade metabasalts; epidote will appear at higher metamorphic grades (Robinson and others, 1993).

Discussion of Deposit-Scale Mapped Mineral Zonation Patterns

A mineral and vegetation group map of the Goldfield mining district, Nevada, was produced from Landsat 8 OLI data acquired on August 1, 2013 (fig. 6). The Goldfield district contains numerous high-sulfidation, quartz-alunite gold deposits of local bonanza grade that are of magmatic-hydrothermal origin (Rye and others, 1992). The deposits typically contain abundant pyrite both in mineralized quartz ledges and in adjacent advanced argillic halos. Surfaces with detected iron sulfate minerals, and thus increased potential NAP, are shown in shades of red. Such surfaces include classes 12, 14, 17, and 18 identified on waste rock piles (F) and tailings deposits (G), as well as mainly undisturbed, quartz-alunite-kaolinite-jarosite ± pyrophyllite rocks (class 9, including at A) (fig. 7). These surfaces correlate well with occurrences of iron sulfate minerals ± other ferric iron minerals identified through analysis of VNIR data acquired by the airborne AVIRIS sensor (Rockwell and others, 2015).

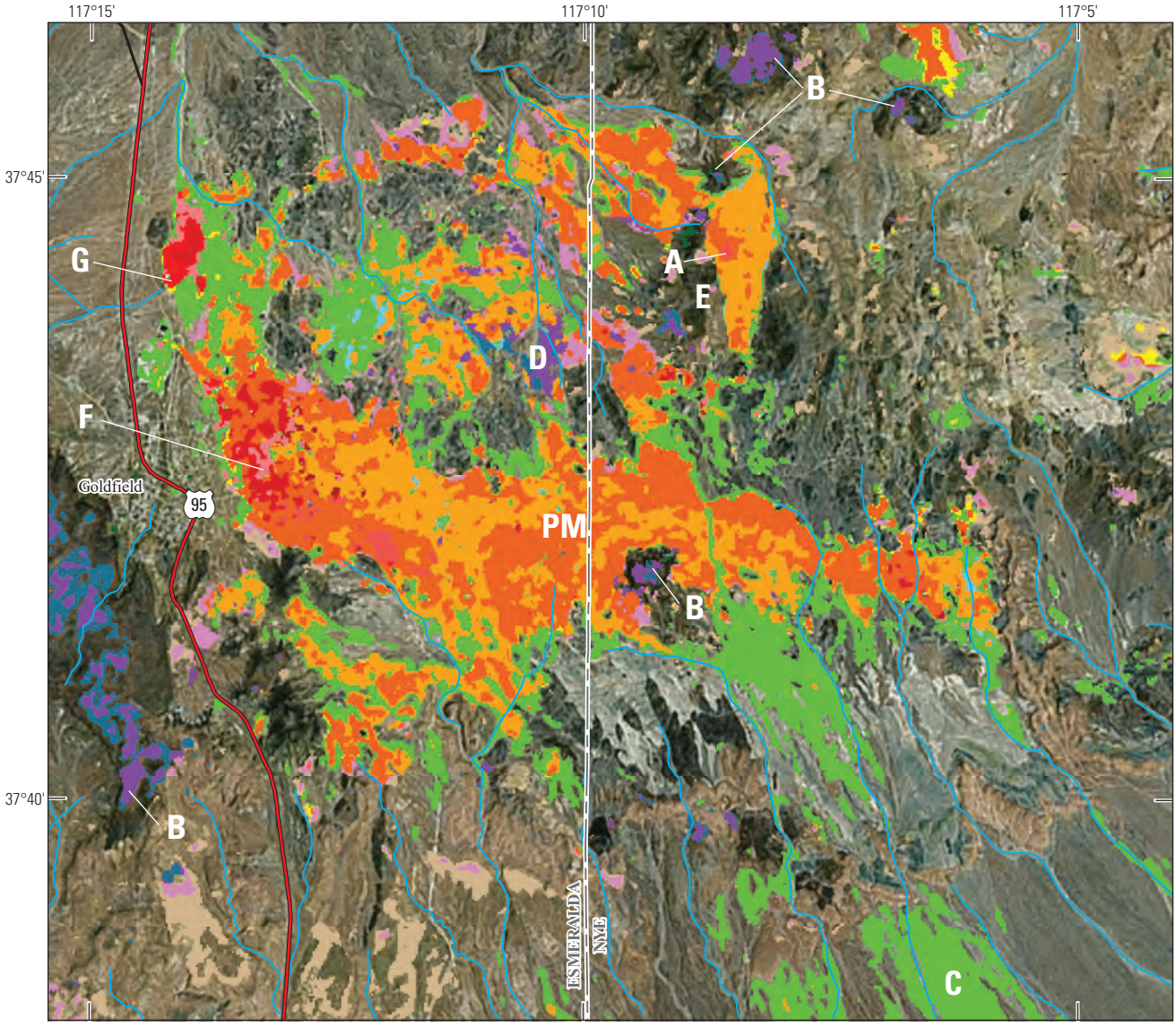

0 1 2 3 MILES
0 1 2 3 KILOMETERS

EXPLANATION

- 14 — Clay, sulfate, mica, and (or) marble with possible oxidizing sulfides and minor iron sulfate, or amorphous iron in playa surfaces and other high-albedo soils
- 12 — Clay, sulfate, mica, and (or) marble + major ferric iron with possible oxidizing sulfides and major iron sulfate
- 17 — Clay, sulfate, mica, and (or) marble + major ferric iron with possible major iron sulfate and hydroxide (commonly proximal zones of weathered, highly pyritic rocks and mine waste)
- 18 — Clay, sulfate, mica,and (or) marble + major ferric iron with possible moderate to major iron sulfate and hydroxide (commonly distal zones of weathered, highly pyritic rocks and mine waste)
- 9 — Clay, sulfate, mica, and (or) marble + major ferric iron with possible iron sulfate and hydroxide (commonly in argillically-altered rocks)
- 19 — Clay, sulfate, mica, and (or) marble + ferrous or coarse-grained ferric iron with possible minor iron sulfate
- 8 — Clay, sulfate, mica, and (or) marble + major ferric iron
- 7 — Clay, sulfate, mica, and (or) marble + moderate to major ferric iron
- 6 — Clay, sulfate, mica, and (or) marble + minor ferric iron
- 2 — Major ferric iron
- 1 — Minor ferric iron (high redness, often includes hematite)
- 3 — Ferric ± ferrous iron
- 5 — Clay, sulfate, mica, and (or) marble
- 4 — Ferrous or coarse-grained ferric iron (may include oxidized basalts, fire ash, some moist soils, and any blue/green rocks)
- Hydrology
- PM — Preble Mountain
- C — Location of significance

Figure 6. Mineral and vegetation group map of the Goldfield mining district, Nevada, generated from Landsat 8 OLI data using the automated algorithm described herein. Class numbers mentioned in the text are shown within the colored boxes in the map explanation (fig. 3). A, exposure of spectrally pure jarosite identified as class 9 within a broader zone of pervasive advanced argillic alteration

in primarily undisturbed rock (Rockwell, 2012); B, hematite-bearing, oxidized Tertiary basalts identified as class 3 or 4; C, alluvium containing alunite and kaolinite derived from weathering of intense advanced argillic alteration in the Goldfield Hills east of the town of Goldfield; D, weakly propylitized rhyolite and quartz latite flows containing muscovite and chlorite identified as class 3 and 4 (ferrous-iron bearing mineral groups), representing abundant chlorite; E, Diamond (Peak); F, highly pyritic waste rock near the Florence Mine; and G, tailings deposits from Consolidated 100-stamp mill in which jarosite with local copiapite were detected using AVIRIS data. PM = Preble Mountain, the highest point in the Goldfield Hills. This map is also available online and can be compared to mineral maps derived from analysis of AVIRIS, ASTER, and Landsat 7 data (Rockwell and others, 2015).

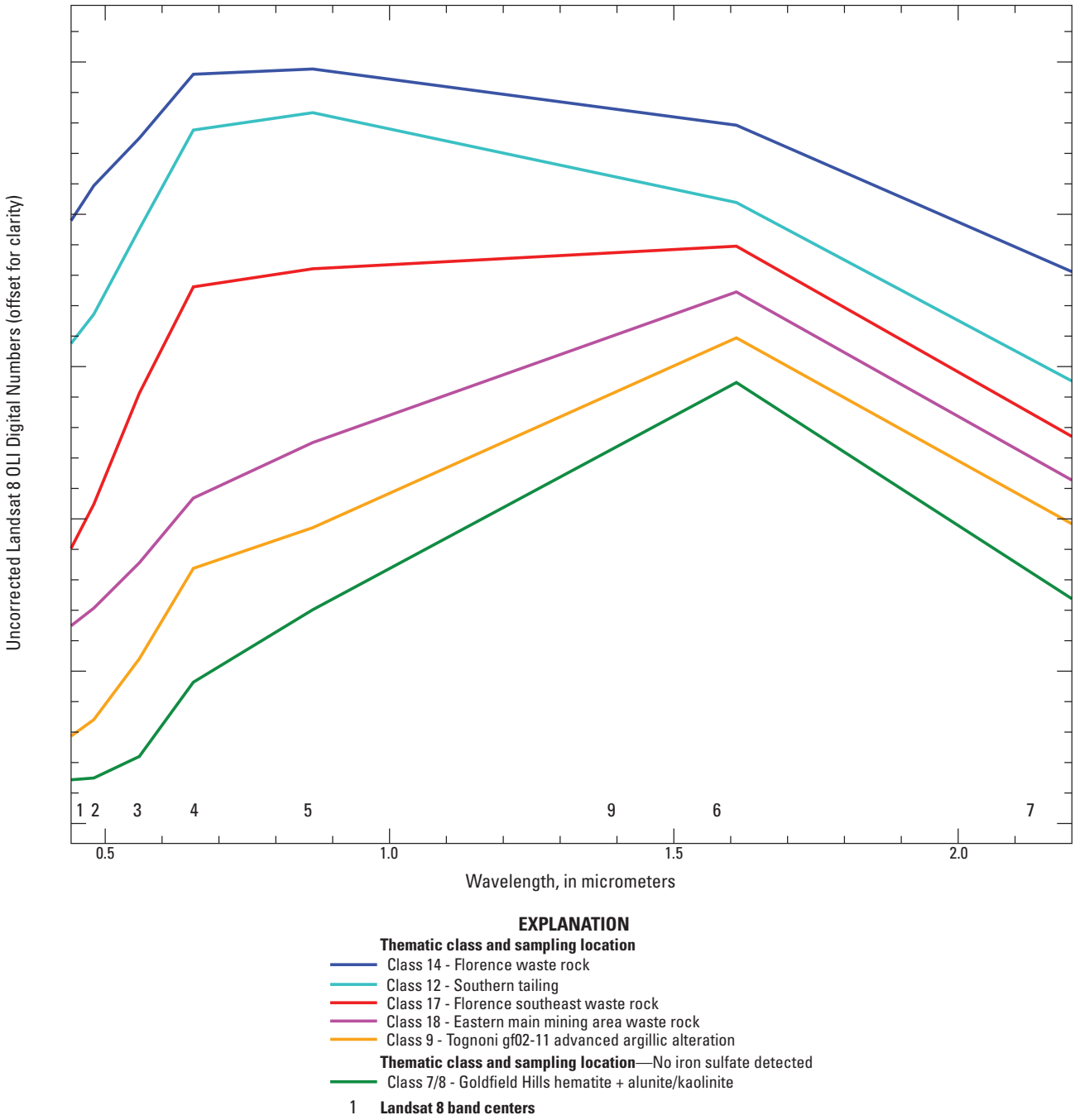

Figure 7. Uncorrected Landsat 8 OLI spectra from scene covering Goldfield, Nevada, collected on August 1, 2013. Class numbers correspond to those shown in figures 3 and 6 and represent the thematic output class of the automated analysis algorithm. The estimated relative NAP, based on interpretation of near-surface pyrite abundance derived from iron sulfate mineral occurrence and comparison with AVIRIS-derived mineral maps, increases from bottom to top. Landsat 8 band centers are shown along the bottom of the plot. Spectra from waste rock were collected from the vicinity of the Florence Mine in the main mining area (location F, fig. 6), and the spectrum of jarosite-bearing, altered rock (classified as class 9, shown in orange) was collected from location A in figure 6. The spectrum shown in dark cyan was sampled from the southern end of the tailings deposit where copiapite and minor jarosite and goethite were identified using AVIRIS data (G, fig. 6). Copiapite is characterized by a slight decrease in reflectance between 0.87 µm (Landsat 8 band 5) and 1.65 µm (Landsat 8 band 6), whereas jarosite typically shows a strong increase (Clark and others, 2007). The spectrum shown in green was sampled from quartz-alunite alteration in the Goldfield Hills east of Preble Mountain (fig. 6) in which no iron sulfate minerals were detected using Landsat 8 data, and hematite was identified using AVIRIS data. Note the flat spectral response between Landsat bands 1 and 2. No units appear on the y-axis because the classes (Landsat 8 OLI Digital Numbers) have been offset for clarity; tic marks remain for horizontal comparison only.

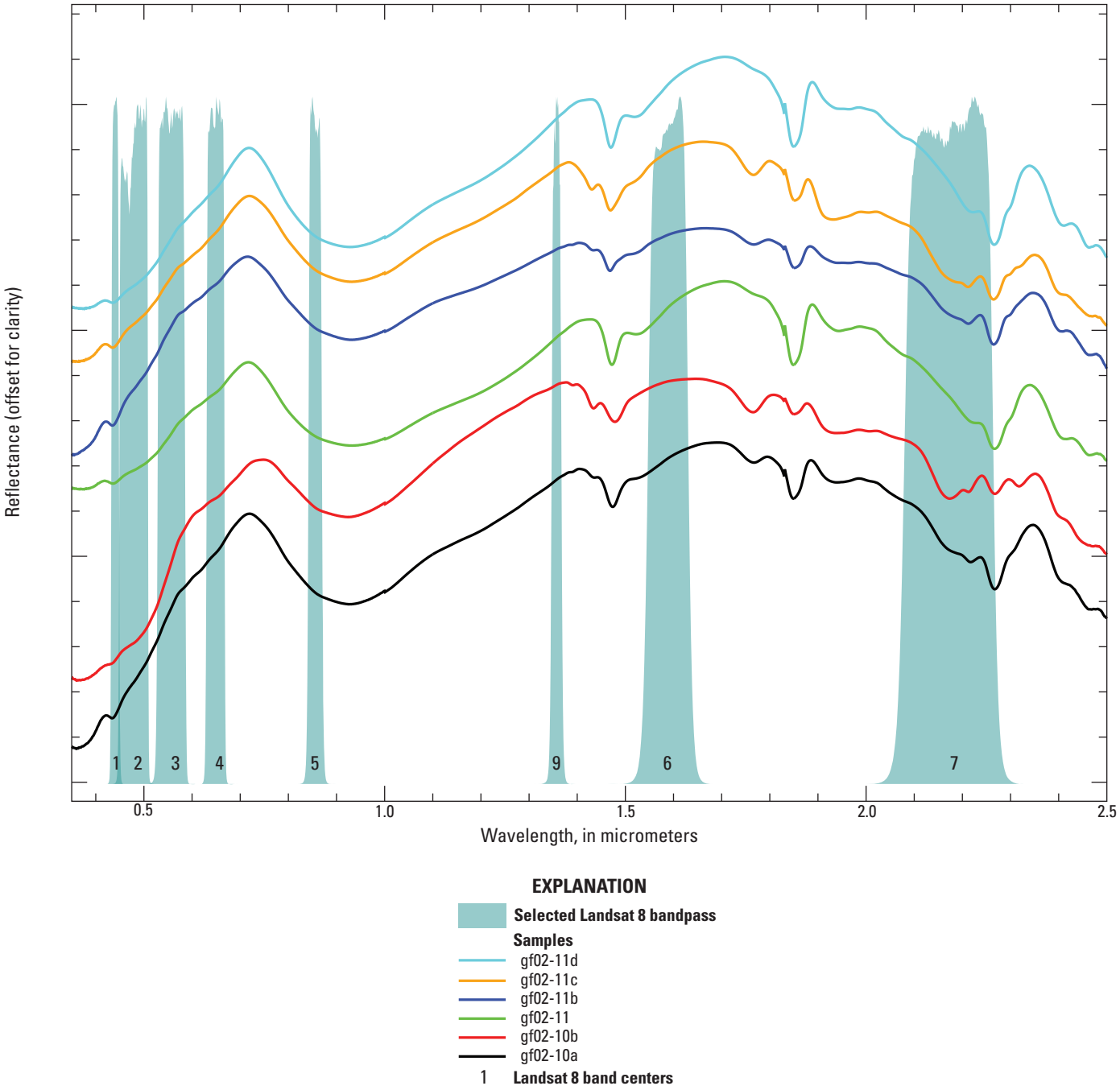

Figure 8. Laboratory reflectance spectra of field samples collected from undisturbed, highly altered rock (fig. 6*A*) east of Diamond (Peak) in the Goldfield mining district, Nevada. All samples contain a mixture of jarosite with minor natrojarosite as determined by bulk X-ray diffraction. Sample gf02-10b (shown in red) contains a mixture of alunite and natroalunite and trace kaolinite. Samples gf02-11b, gf02-11c, and gf02-10a contain trace alunite and kaolinite. Sample locations (WGS84 datum): gf02-10 (117.14436°W, 37.74255°N), gf02-11 (117.14280°W, 37.74138°N). No units appear on the y-axis because the classes (reflectance from plotted samples) have been offset for clarity; tic marks remain for horizontal comparison only.

In the Goldfield district, undisturbed rocks in which jarosite was detected have several distinctive spectral features that differentiate them from mine waste and tailings (fig. 8). In addition to the deep absorptions at band 1 (ferric iron) and band 7 (Fe-OH and Al-OH, table 2, figs. 1 and 2) typical of jarosites, these rocks have high reflectance at band 6 and a deep, wide crystal field electronic transition feature related to ferric iron near 1.00 µm (band 5, 0.85 – 0.88 µm, table 2) (fig. 7). These NIR spectral features result in high values for a Landsat (3+6) / (4+5) compound band ratio (ferric iron index 2, tables 3 and 4) for the altered rocks, and may indicate larger grain size (Clark, 1999; Rockwell, 2004). These surfaces were identified primarily as class 9 and are usually underlain by undisturbed, highly altered pyritic rock containing abundant clay, sulfate, and (or) mica minerals (in this case alunite, kaolinite, and jarosite with local pyrophyllite). The iron minerals in these rocks generally have coarser grain sizes than the fine-grained jarositic coatings commonly found on weathered, pyritic waste rock and tailings (Swayze and others, 2000; Rockwell and others, 2005).

Tailings deposits of the Bauer Mill located 2.3 km north of Stockton, Utah, were an important site for development and testing of the Landsat 8 data analysis algorithm becausethe site is within an area covered by detailed mineral maps derived from analysis of AVIRIS data (Rockwell and others, 2005). Between 1900 and 1957, the Bauer Mill processed sulfide-rich ores derived from the polymetallic vein and replacement deposits of the Stockton mining district in the western Oquirrh Mountains. The mineralogy of the tailings shows a marked change with increased distance from the mill; grading from weathered pyrite near the mill to zones of jarosite, jarosite + goethite, goethite, and hematite in distal eolian deposits deposited to the north of the tailings by the prevailing southerly winds. Figure 9 shows mineral maps of the Bauer Mill site derived from analysis of high-altitude AVIRIS and Landsat 8 OLI data. Similar patterns of mineralogic variation relative to the mill site are evident in both maps.

Figure 10 shows averaged spectra of uncorrected Landsat 8 OLI digital numbers of the Bauer Mill tailings sampled from areas classified as particular mineral classes by the analysis algorithm. Averaged AVIRIS reflectance spectra sampled from the same general locations are shown in figure 11. In both spectral plots, the spectra of weathered pyrite (black) sampled close to the mill site show low overall reflectance (especially near 1.65 µm, Landsat 8 OLI band 6) and decreased absorption near 0.44 µm relative to the red wavelengths (approximately 0.65 µm) compared with the spectra of more distal, jarositic tailings classified as classes 12 and 17. These differences in the visible region are related to the dark gray color of the proximal pyritic material compared to the yellowish color of the more distal, jarositic material. Spectra of material with more abundant goethite (green) and hematite (blue) show flat to negative slopes between Landsat 8 bands 1 and 2, contrasting with the strongly positive slope in the spectra of the jarositic and pyritic tailings.

Known occurrences of iron sulfate minerals in several other locations in the western U.S. were accurately identified using the Landsat 8 OLI data analysis. In the Antelope Range of the Marysvale volcanic field, Utah, iron sulfate minerals were identified only in phyllic alteration exposed by the downcutting of the Sevier River beneath Miocene steam-heated alunite deposits (fig. 12). Mixtures of jarosite + illite + gypsum ± clay minerals were identified in these highly pyritic rocks using AVIRIS data (Cunningham and others, 2005; Rockwell and others, 2005, 2015). Other altered volcanic rocks and related alluvium containing abundant clay, sulfate, mica, and (or) hematite and goethite are clearly visible surrounding the central monzonite intrusion in the Landsat 8-derived material map.

Iron sulfate minerals were also identified in highly pyritic and jarositic mine waste and tailings at other sites including the following:

- waste rock along the eastern side of the main open pit of the Bingham Canyon mine in the eastern Oquirrh Mountains of Utah. Abundant jarosite and possible copiapite, alunogen, and epsomite were identified in this mine waste using high-altitude AVIRIS data (Rockwell and others, 2005);
- several piles of pyritic and jarositic mine waste in the Leadville mining district, Colorado (Swayze and others, 2000; Rockwell and others, 2013b);
- jarositic tailings material at the Argo Mill in Idaho Springs, Colorado (Rockwell and others, 2013b);
- jarositic tailings, mine waste, and altered wall rock at the Climax molybdenum mine near Leadville, Colorado (Rockwell and others, 2013b);
- jarositic mine waste rock at the Swansea and Dragon Mines, and in mill tailings near the Burgin Mine, in the Tintic mining district, Utah (Rockwell and others, 2005); and
- jarositic cements and related colluvium in Jurassic Navajo Sandstone at Mollie's Nipple in southern Utah (Bell and others, 2010; Rockwell and others, 2015).

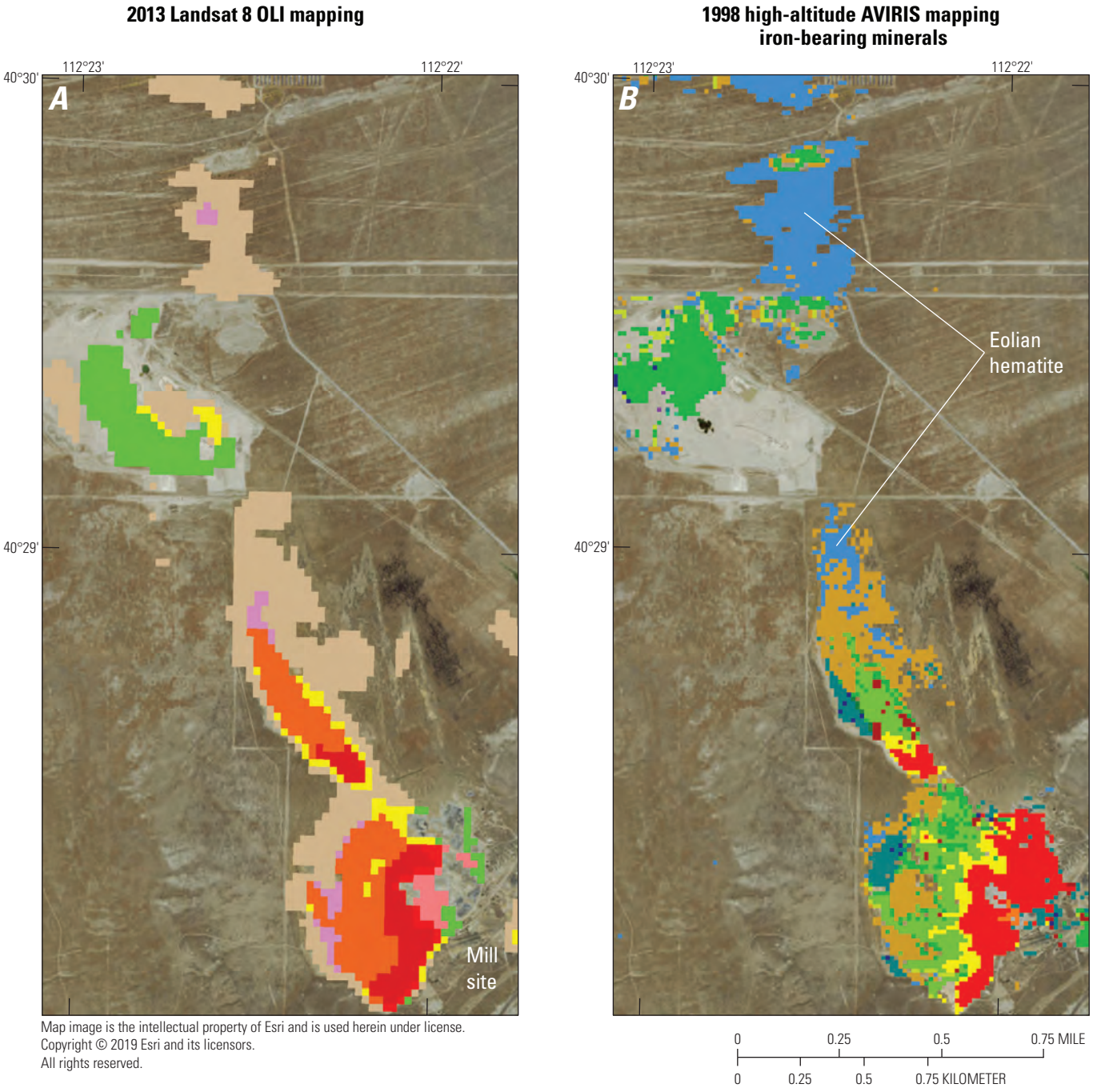

Figure 9. Mineral maps of the Bauer Mill site near Stockton, Utah, derived from analysis of *A*. Landsat 8 OLI data and *B*. high-altitude AVIRIS data. Explanation for color-coded analysis results of Landsat 8 OLI-based mapping is shown at bottom. Color-coded mineral identifications for AVIRIS-derived results (not shown in map explanation): orange = weathered pyrite, red = fine-grained jarosite, dark red = coarse-grained jarosite, yellow = jarosite + goethite, green = goethite, light blue = hematite, light brown = minerals with generic ferric iron absorptions, dark cyan = minerals with generic ferrous iron absorptions. AVIRIS-derived results (Rockwell and others, 2005) have a 17-meter ground pixel size and can be compared with the Landsat 8-derived results and other data in the National Map of Surficial Mineralogy (Rockwell and others, 2015). Landsat 8 data shown here were acquired on June 9, 2013, and AVIRIS data were acquired on August 5, 1998. The location of the mill site from which the tailings emanated is shown.

Figure 9. Mineral maps of the Bauer Mill site near Stockton, Utah, derived from analysis of *A*. Landsat 8 OLI data and *B*. high-altitude AVIRIS data. Explanation for color-coded analysis results of Landsat 8 OLI-based mapping is shown at bottom. Color-coded mineral identifications for AVIRIS-derived results (not shown in map explanation): orange = weathered pyrite, red = fine-grained jarosite, dark red = coarse-grained jarosite, yellow = jarosite + goethite, green = goethite, light blue = hematite, light brown = minerals with generic ferric iron absorptions, dark cyan = minerals with generic ferrous iron absorptions. AVIRIS-derived results (Rockwell and others, 2005) have a 17-meter ground pixel size and can be compared with the Landsat 8-derived results and other data in the National Map of Surficial Mineralogy (Rockwell and others, 2015). Landsat 8 data shown here were acquired on June 9, 2013, and AVIRIS data were acquired on August 5, 1998. The location of the mill site from which the tailings emanated is shown.—Continued

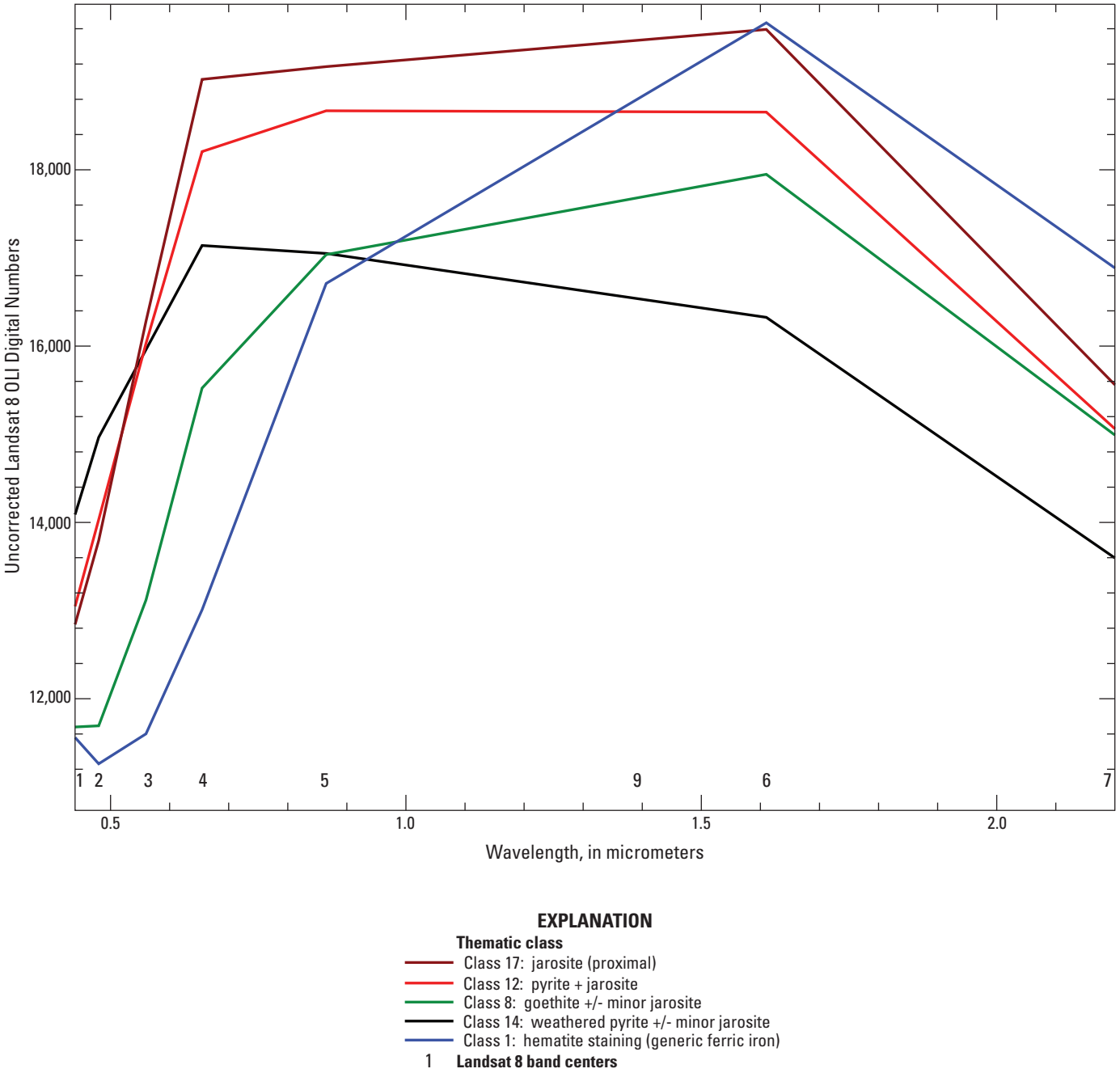

Figure 10. Average spectra of Landsat 8 OLI data from tailings deposits at the Bauer Mill site. Spectra represent averages of several pixels classified as a particular class. Note flat to negative slope between Landsat 8 bands 1 and 2 in the spectra of surfaces spectrally dominated by goethite and hematite.

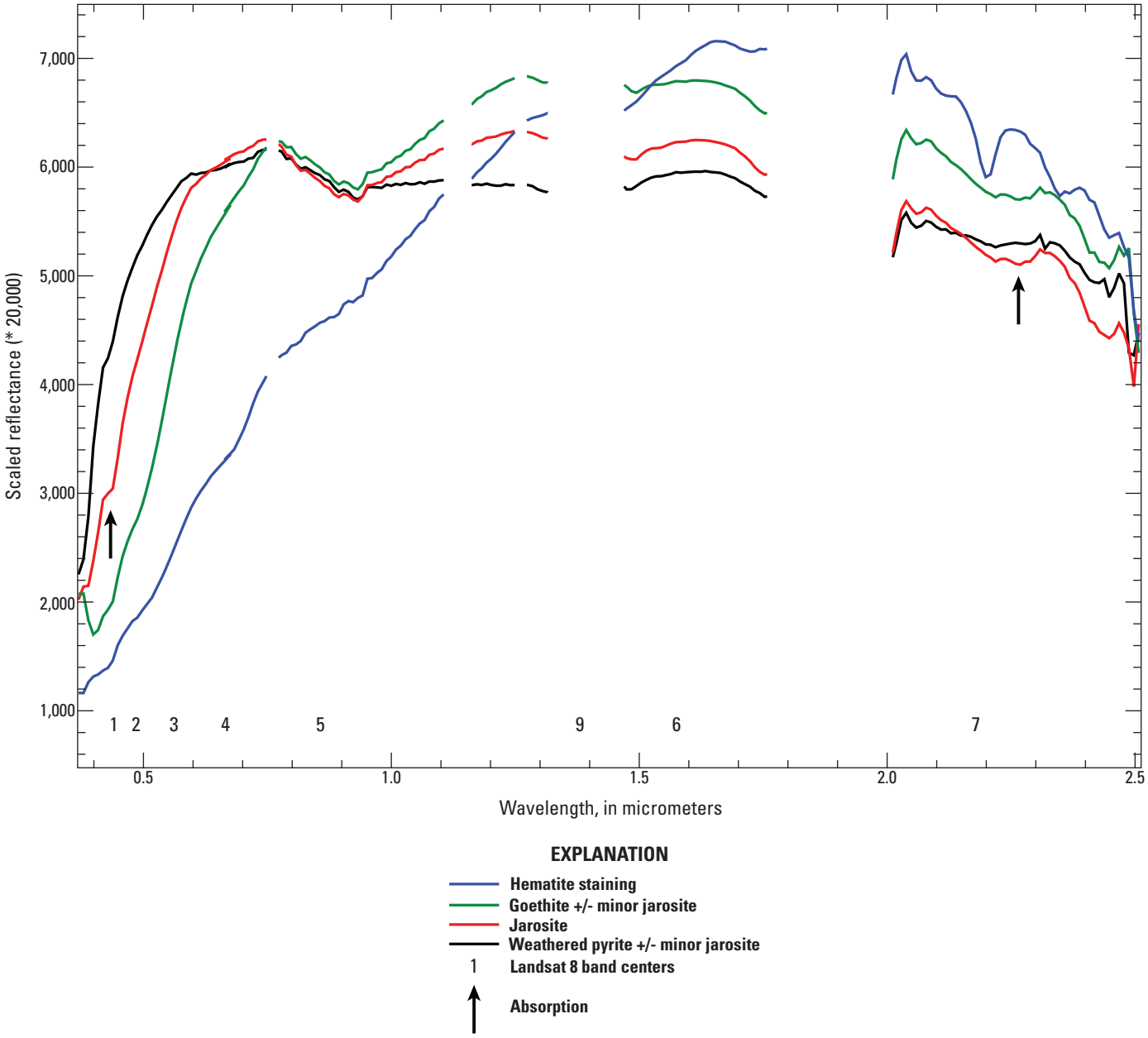

Figure 11. Average spectra of high-altitude AVIRIS data from tailings deposits at the Bauer Mill site sampled from the same general locations as the spectra in figure 10, using matching colors for the same sampling locations. Spectra represent averages of several pixels classified as a particular mineral or mineral mixture. Arrows indicate absorptions at 0.43 and 2.27 micrometers [µm] related to jarosite. These jarosite absorptions are deepest in the spectrum of jarositic tailings (red) sampled just down-gradient (northwest) from the mapped exposure of weathered pyrite (black) nearest the mill site.

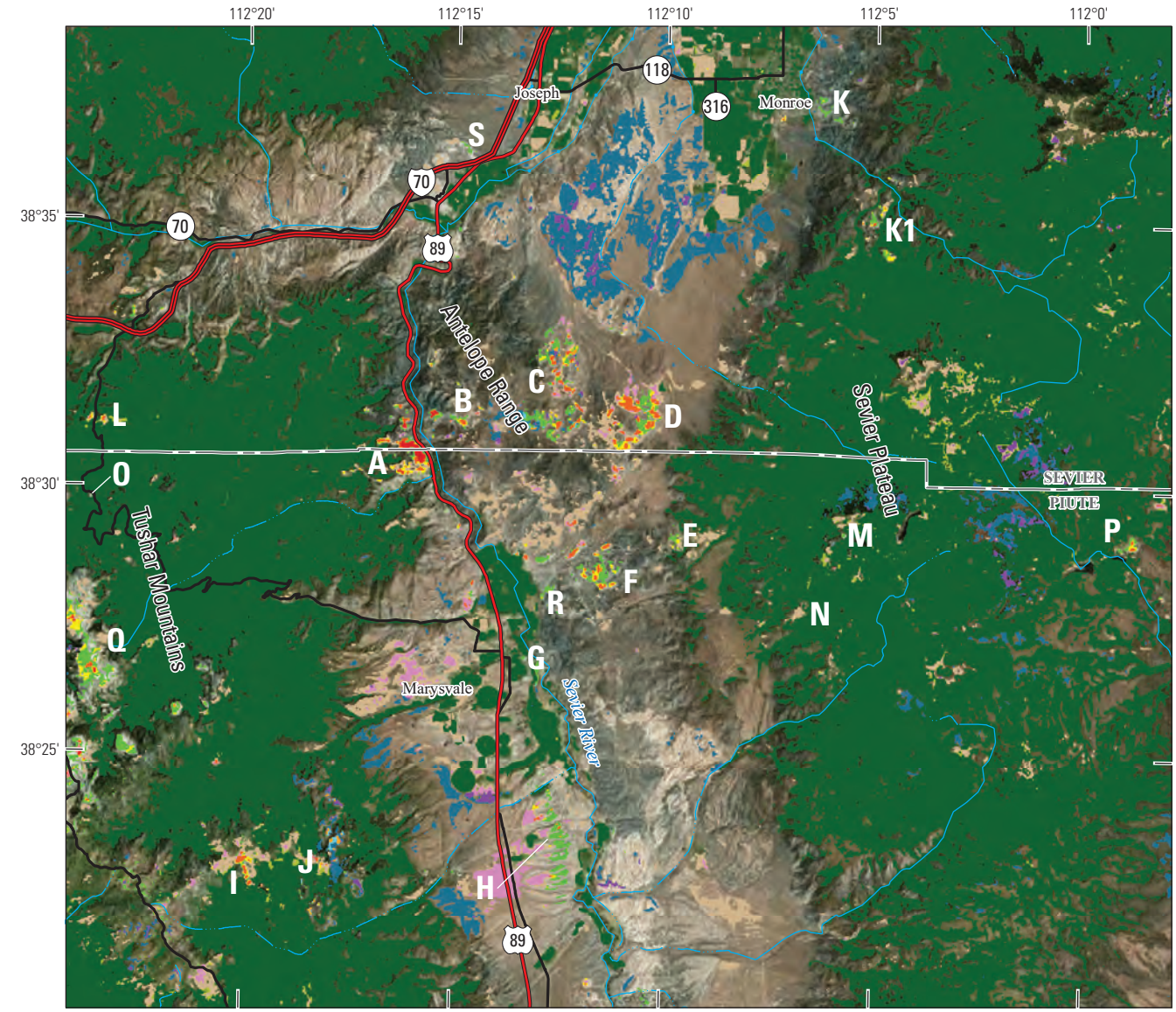

EXPLANATION

11	Dense, green vegetation
14	Clay, sulfate, mica, and (or) marble with possible oxidizing sulfides and minor iron sulfate, or amorphous iron in playa surfaces and other high-albedo soils
12	Clay, sulfate, mica, and (or) marble + major ferric iron with possible oxidizing sulfides and major iron sulfate
17	Clay, sulfate, mica, and (or) marble + major ferric iron with possible major iron sulfate and hydroxide (commonly proximal zones of weathered, highly pyritic rocks and mine waste)
18	Clay, sulfate, mica,and (or) marble + major ferric iron with possible moderate to major iron sulfate and hydroxide (commonly distal zones of weathered, highly pyritic rocks and mine waste)
9	Clay, sulfate, mica, and (or) marble + major ferric iron with possible iron sulfate and hydroxide (commonly in argillically-altered rocks)
19	Clay, sulfate, mica, and (or) marble + ferrous or coarse-grained ferric iron with possible minor iron sulfate
8	Clay, sulfate, mica, and (or) marble + major ferric iron
7	Clay, sulfate, mica, and (or) marble + moderate to major ferric iron
6	Clay, sulfate, mica, and (or) marble + minor ferric iron
2	Major ferric iron
1	Minor ferric iron (high redness, often includes hematite)
3	Ferric ± ferrous iron
5	Clay, sulfate, mica, and (or) marble
4	Ferrous or coarse-grained ferric iron (may include oxidized basalts, fire ash, some moist soils, and any blue/green rocks)
	Hydrology
C	Location of significance

Figure 12. Mineral group map of the northern Marysvale volcanic field, Utah, generated from Landsat 8 OLI data using the automated algorithm described herein. A, steam-heated advanced argillic (alunite, pyrophyllite), argillic (kaolinite, dickite), and phyllic alteration (iron sulfate minerals identified) associated with Big Rock Candy Mountain replacement alunite deposit; B, Big Star natroalunite deposit

showing iron sulfate minerals identified on lower, western flanks of deposit near Sevier River, correlating well with mineral mapping results derived from analysis of low- and high-altitude AVIRIS data (Rockwell and others, 2005); C, Yellow Jacket alunite deposit; D, Al Kee Mee alunite deposit; E, White Hills alunite deposit; F, White Horse alunite deposit (Rockwell, 2009); G, alunitic waste rock at loading site (approximately 80-100 m in diameter) on outskirts of town of Marysvale identified as class 5; H, alluvium bearing alunite, kaolinite, and ferric iron minerals derived from weathering of altered areas on Alunite Ridge and Deer Trail Mountain (Rockwell and others, 2005); I, Alunite Ridge magmatic steam alunite deposit; J, argillic alteration on summit of Deer Trail Mountain; K, kaolinite with possible minor alunite associated with Monroe hot springs; K1, possible phyllic alteration with kaolinite identified in northern area using ASTER data (Rockwell, 2009, 2012) and iron sulfate minerals (classes 12 and 14) identified using the Landsat 8 data analysis (iron sulfate minerals not field-verified at this location), and alunitic rocks with local minor ferric iron minerals to south mapped as classes 5 and 6; L, Red Narrows kaolinite mines with hematite (mined for fire brick) mapped as classes 1, 6, and 8; M, Marysvale Peak alunite deposit mapped as class 5; N, Aluminum Queen alunite deposit; O, several pixels of class 1 (minor ferric iron) mapped in tailings from mill, Kimberly mining district; P, Box Creek kaolinite deposit; Q, sericite, smectite, and minor kaolinite associated with weak argillic and regional propylitic alteration of Big John caldera fill; R, argillic alteration (kandite clay) associated with Saturday uranium prospect in northern Bullion Hills; S, smectite in lacustrine deposits of the Sevier River Formation identified primarily as class 5 (table 4). This map is also available online and can be compared to mineral maps derived from analysis of AVIRIS, ASTER, and Landsat 7 data (Rockwell and others, 2015).

Deficiencies of the Automated Analysis Methodology

For the regional mapping program, an effort was made to select Landsat 8 scenes with minimal cloud and snow cover and optimal solar illumination for processing and analysis. However, suitable Landsat data were not available for all areas. Some scenes with unclear atmosphere caused by dust, haze, clouds, fog, and smoke were the best available, and these showed uncertain analysis results. Clouds and related cloud shadows were manually masked and assigned as class 15 (No Data), most often after data analysis. Other surface features and conditions can also affect the quality of the analysis. False mineral group detections can also occur in areas where abundant lichen and (or) seasonally dry, yellow to brown vegetation such as cheatgrass is present, especially in the northern Great Basin, and in fallow agricultural fields. High soil moisture contents will darken the land surface leading to incomplete or erroneous results.

Landsat 8 OLI data analysis will not generally identify exposures of carbonate and Mg-OH minerals, except in cases of recrystallization where carbonate mineral abundance is increased (for example, marble) or when phyllosilicate minerals are also present. This is because of the spectral coverage of Landsat 8 OLI band 7 with respect to the diagnostic absorptions of these minerals. Additionally, vegetative cover is more common over carbonate-bearing rocks and soils in semiarid regions than over quartz-rich rock types and argillically and pyritically altered rocks (Rockwell and Hofstra, 2008), which also makes carbonate and Mg-OH minerals less likely to be identified. Vegetation suppression logic was applied to the Landsat 8 clay-sulfate-mica-marble index, in which 5/4 ratio results were subtracted from 6/7 ratio results to generate a clay-sulfate-mica-marble index (table 3) (Rockwell, 2013a). This methodology is more likely to remove pixels from the clay-sulfate-mica-marble index in areas where carbonate and (or) Mg-OH minerals are present. These features of Landsat data and the analysis technique will tend to skew results by overrepresenting potentially acid-producing argillic and phyllic alteration and underrepresenting potentially acid-neutralizing rocks and soils. However, as the identification of potentially acid-producing rocks is one of the most important objectives of the mapping, this is not a fatal flaw of the methodology. Mineral maps derived from analysis of ASTER reflective data can be used for identification of carbonate and Mg-OH minerals over broad regions (Rockwell, 2012; Rockwell and others, 2015), and ASTER thermal infrared data can be used to identify thick carbonate units (Rockwell and Hofstra, 2008).

In relatively rare cases, undisturbed, hydrothermally altered rocks containing clay, sulfate, and (or) mica minerals are partially covered by green vegetation. If the vegetative cover is sufficiently dense, the vegetation suppression logic may remove most or all pixels from the clay-sulfate-mica-marble index. Therefore, if any pixels of this index are mapped in an area with vegetative cover, field checking and (or) additional data analysis should be performed to understand the true extent of altered rocks. Customized Landsat analysis without vegetation suppression, or ASTER data analysis, can be used as verification tools in such cases.

As described by Rockwell (2012) regarding the automated ASTER data analysis technique, any ratio-based spectral analysis algorithm will present “answers” for every material index. Even if no minerals of a type for which an index was designed are present in a scene, the high-end values of that index will be shown as a detection result. Therefore, the results of ratio-based analysis algorithms represent “high likelihood” maps where a particular material is most likely to occur. For the regional analysis (Rockwell and others, 2015), occurrences of the iron sulfate classes (12, 17, and 18) within agricultural areas were changed to classes 16, 20, and 21, respectively, and assigned the label “clay, sulfate, mica, and/or marble + ferric iron ± sparse, green vegetation, including fallow agricultural fields (class X),” where X is the number of the originally identified iron sulfate mineral class.

Landsat scenes are analyzed on a scene-by-scene basis. Since scene-wide statistics are used to calculate the values used for clipping the low-end values of each index, material identifications across scene boundaries will not always be continuous. In addition, seasonal and annual variation between adjacent scenes collected on different dates may cause visible variation in mapped materials in scene overlap areas related to changes in vegetation abundance and dryness, soil moisture content, and atmospheric conditions.

Conclusions

The products generated by the automated process are ideal for efficient application to mineral resources and geoenvironmental assessments at regional and national scales. The addition of new L8 band + band index results in a more ‘robust’ identification of iron sulfate minerals produced by weathering and oxidation of pyrite. Consequently, the products of this improved methodology can be used as a low-cost, preliminary screening tool to focus field sampling programs aimed at identifying pyritic, altered rocks in frontier areas and to identify potential sources of acid rock drainage. Despite deficiencies in the quality and availability of Landsat 8 OLI data, the improved methodology offers finer spectral discrimination compared to the Landsat 7 ETM. However, integrating the Landsat-derived results with geologic maps and mineral maps generated from analysis of ASTER data or hyperspectral sensors is expected to yield an optimal, hybrid map of hydrothermally altered areas. Integration of available tools improves accuracy and allows for detailed characterization of alteration types.

Acknowledgments

The author would like to thank the U.S. Geological Survey Earth Resources Observation and Science Center (EROS) for providing the Landsat 8 data, and Greg Fernette, Douglas Yager, and Bernard Hubbard of the U.S. Geological Survey for their helpful reviews of the manuscript, maps, and digital data.

References Cited

Bell, J.H., Bowen, B.B., and Martini, B.A., 2010, Imaging spectroscopy of jarosite cement in the Jurassic Navajo Sandstone: Remote Sensing of Environment, v. 114, no. 10, p. 2259–2270, accessed May 27, 2016, at https://doi.org/10.1016/j.rse.2010.05.002.

Bohannon, R.G., and Meier, A.L., 1976, Lithium in sediments and rocks in Nevada: U.S. Geological Survey Open-File Report 76–567, 17 p. [Also available at https://doi.org/10.3133/ofr76567.]

Bove, D.J., Rye, R.O., and Hon, K. 1990, Evolution of the Red Mountain alunite deposit, Lake City, Colorado: U.S. Geological Survey Open-File Report 90–235, 32 p. [Also available at https://doi.org/10.3133/ofr90235.]

Bove, D.J., Yager, D.B., Mast, M.A., and Dalton, J.B., 2007, Alteration map showing major faults and veins and associated water-quality signatures of the Animas River watershed headwaters near Silverton, southwest Colorado: U.S. Geological Survey Scientific Investigations Map 2976, 1 plate, scale 1:24,000, 18-p. pamphlet, accessed June 16, 2016 at https://doi.org/10.3133/sim2976.

Briggs, P.H., and Meier, A.L., 2002, The determination of forty-two elements in geological materials by inductively coupled plasma-mass spectrometry, *in* Taggart, J.E., Jr., ed., Analytical methods for chemical analysis of geologic and other materials, U.S. Geological Survey: U.S. Geological Survey Open-File Report 02–223, p. I1-I14, accessed October 25, 2016, at http://pubs.usgs.gov/of/2002/ofr-02-0223/I20NAWQAPlus_M.pdf.

Chavez, P.S., Jr., 1988, An improved dark-object subtraction technique for atmospheric scattering correction of multispectral data: Remote Sensing of Environment, v. 24, no. 3, p. 459–479. [Also available at https://doi.org/10.1016/0034-4257(88)90019-3.]

Church, S.E., Fey, D.L., Klein, T.L., Schmidt, T.S., Wanty, R.B., DeWitt, E.H., Rockwell, B.W., and San Juan, C.A., 2009, Environmental effects of hydrothermal alteration and historical mining on water and sediment quality in central Colorado, *in* Webb, R.M.T., and Semmens, D.J., eds., Planning for an uncertain future—Monitoring, integration, and adaptation. Proceedings of the Third Interagency Conference on Research in the Watersheds: U.S. Geological Survey Scientific Investigations Report 2009–5049, 292 p., accessed June 16, 2016 at https://pubs.usgs.gov/sir/2009/5049/.

Clark, R.N., 1999, Spectroscopy of rocks and minerals, and principles of spectroscopy, *in* Rencz, A.N., and Ryerson, R.A., eds., Remote Sensing for the Earth Sciences, Manual of Remote Sensing: New York, John Wiley & Sons, Inc., v. 3, p. 3–58.

Clark, R.N., Swayze, G.A., Wise, R.A., Livo, E.K., Hoefen, T.M., Kokaly, R.F., and Sutley, S.J., 2007, USGS digital spectral library splib06a: U.S. Geological Survey Digital Data Series 231, accessed October 25, 2016, at http://speclab.cr.usgs.gov/spectral.lib06.

Crippen, R.E., 1989, Selection of Landsat TM band and band-ratio combinations to maximize lithologic information in color composite displays, *in* Proceedings of the Thematic Conference on Geologic Remote Sensing, Seventh thematic conference on Remote sensing for exploration geology, Calgary, AB, Canada, Oct. 2–6, 1989, ERIM: Ann Arbor, Michigan, USA, p. 917–921.

Crowley, J.K., Brickey, D.W., and Rowan, L.C., 1989, Airborne imaging spectrometer data of the Ruby Mountains, Montana—Mineral discrimination using relative absorption band-depth images: Remote Sensing of Environment, v. 29, p. 121–134. [Also available at https://doi.org/10.1016/0034-4257(89)90021-7.]

Crowley, J.K., Williams, D.E., Hammarstrom, J.M., Piatak, N., Chou, I-Ming, and Mars, J.C., 2003, Spectral reflectance properties (0.4–2.5 μm) of secondary Fe-oxide, Fe-hydroxide, and Fe-sulphate-hydrate minerals associated with sulphide-bearing mine wastes: Geochemistry Exploration Environment Analysis, v. 3, p. 219–228, accessed June 16, 2016 at https://doi.org/10.1144/1467-7873/03-001.

Cunningham, C.G., Rye, R.O., Rockwell, B.W., Kunk, M.J., and Councell, T.B., 2005, Supergene destruction of a hydrothermal replacement alunite deposit at Big Rock Candy Mountain, Utah—Mineralogy, spectroscopic remote sensing, stable isotope and argon age evidences: Chemical Geology, v. 215, no. 1–4, p. 317–337, accessed October 10, 2016 at https://doi.org/10.1016/j.chemgeo.2004.06.055.

Dalton, J.B., Bove, D.J., and Mladinich, C.S., 2005, Remote sensing characterization of the Animas River watershed, southwestern Colorado, by AVIRIS imaging spectroscopy: U.S. Geological Survey Scientific Investigations Report 2004–5203, 54 p., accessed October 10, 2016 at https://doi.org/10.3133/sir20045203.

Dalton, J.B., Bove, D.J., Mladinich, C.S., and Rockwell, B.W., 2007, Imaging spectroscopy applied to the Animas River watershed and Silverton Caldera, *in* Church, S.E., von Guerard, P., and Finger, S.E., eds., Integrated investigations of environmental effects of historical mining in the Animas River watershed, San Juan County, Colorado: U.S. Geological Survey Professional Paper 1651, p. 143–159, accessed June 12, 2016, at https://pubs.usgs.gov/pp/1651/.

Day, W.C., Frost, T.P., Hammarstrom, J.M., and Zientek, M.L., eds., 2016, v. 2016–5089. Mineral resources of the sagebrush focal areas of Idaho, Montana, Nevada, Oregon, Utah, and Wyoming, U.S. Geological Survey Scientific Investigations Report 2016–5089, accessed October 10, 2016 at https://doi.org/10.3133/sir20165089.

Elvidge, C.D., and Lyon, R.J.P., 1985, Estimation of vegetation contribution to the 1.65/2.22 μm ratio in the airborne TM imagery of the Virginia Range, Nevada: International Journal of Remote Sensing, v. 6, p. 137–155. [Also available at https://doi.org/10.1080/01431168508948425.]

Horton, J.D., San Juan, C.A., and Stoeser, D.B., 2017, The State Geologic Map Compilation (SGMC) Geodatabase for the Conterminous United States: U.S. Geological Survey Data Series, v. 1052, accessed October 10, 2016 at https://doi.org/10.3133/ds1052.

John, D.A., Rockwell, B.W., Henry, C.D., and Colgan, J.P., 2010, Hydrothermal alteration of the late Eocene Caetano ash-flow caldera, north-central Nevada—A field and ASTER remote sensing study, *in* Steininger, R., and Pennell, B., eds., Great Basin evolution and metallogeny: Geological Society of Nevada Symposium, Reno, Nev., May 14–22, 2010: Geological Society of Nevada 2010 Symposium Volume, p. 1055–1083.

Kaufman, Y.J., 1989, The atmospheric effect on remote sensing and its correction, *in* Asrar, G., ed., Theory and Application of Optical Remote Sensing: New York, Wiley-Interscience, p. 336–428.

Knepper, D.H., Jr., 1989, Mapping hydrothermal alteration with Landsat Thematic Mapper data, *in* Lee, K., Knepper, D.H., Jr., Kruse, F.A., Marrs, R.W., and Milton, N.M., eds., Remote Sensing in Exploration Geology—Golden, Colorado to Washington D.C., June 30–July 8, 1989, Field Trip Guidebook, v. T182, p. 13–21, AGU, Washington, D.C. [Also available at https://agupubs.onlinelibrary.wiley.com/doi/book/10.1029/FT182.]

Knepper, D.H., Jr., 2010, Distribution of potential hydrothermally altered rocks in central Colorado derived from Landsat Thematic Mapper data—A geographic information system data set: U.S. Geological Survey Open-File Report 2010–1076, 14 p., accessed October 10, 2016 at https://doi.org/10.3133/ofr20101076.

Kokaly, R.F., 2011, Detecting cheatgrass on the Colorado Plateau using Landsat data—A tutorial for the DESI software: U.S. Geological Survey Open-File Report 2010–1327, 88 p., accessed October 10, 2016 at https://doi.org/10.1016/j.rse.2006.08.006.

Kokaly, R.F., Rockwell, B.W., Haire, S.L., and King, T.V.V., 2006, Characterization of post-fire surface cover, soils, and burn severity at the Cerro Grande fire, New Mexico, using hyperspectral and multispectral remote sensing: Remote Sensing of Environment, v. 106, no. 3, p. 305–325, accessed October 10, 2016 at https://doi.org/10.1016/j.rse.2006.08.006.

Long, K.R., DeYoung, J.H., Jr., and Ludington, S.D., 1998, Database of significant deposits of gold, silver, copper, lead, and zinc in the United States: U.S. Geological Survey Open-File Report 98–206–A, B, 33 p. [Also available at https://doi.org/10.3133/ofr98206AB.]

Mars, J.C., 2013, Hydrothermal alteration maps of the central and southern Basin and Range province of the United States compiled from Advanced Spaceborne Thermal Emission and Reflection Radiometer (ASTER) data (ver. 1.1, April 8, 2014): U.S. Geological Survey Open-File Report 2013–1139, 5 p., 13 plates, scale 1:1,300,000, https://doi.org/10.3133/ofr20131139.

Ringrose, C.R., 1982, Geology, geochemistry, and stable isotope studies of a porphyry-style hydrothermal system, west Silverton district, San Juan Mountains, Colorado: Aberdeen, Scotland, University of Aberdeen, Ph.D. dissertation, 257 p., 19 plates.

Robinson, D., Bevins, R.E., and Rowbotham, G., 1993, The characterization of mafic phyllosilicates in low-grade metabasalts from eastern North Greenland: The American Mineralogist, v. 78, p. 377–390.

Rockwell, B.W., 1989, Hydrothermal alteration mapping in spectral ratio feature space using TM reflectance data: Aurora mining district, Mineral County, Nevada, *in* Proceedings of the Thematic Conference on Geologic Remote Sensing, Seventh thematic conference on Remote sensing for exploration geology, Calgary, AB, Canada, Oct. 2–6, 1989, ERIM: Ann Arbor, Michigan, USA, p. 1189–1203.

Rockwell, B.W., 2004, Spectral variations in rocks and soils containing ferric iron hydroxide and(or) sulfate minerals as seen by AVIRIS and laboratory spectroscopy: U.S. Geological Survey Open-File Report 2004–1431, 24 p., accessed October 10, 2016 at https://doi.org/10.3133/ofr20041431.

Rockwell, B.W., 2009, Comparison of ASTER- and AVIRIS-derived mineral and vegetation maps of the White Horse replacement alunite deposit and surrounding area, Marysvale volcanic field, Utah: U.S. Geological Survey Scientific Investigations Report 2009–5117, 31 p., accessed October 10, 2016 at https://doi.org/10.3133/sir20095117.

Rockwell, B.W., 2012, Description and validation of an automated methodology for mapping mineralogy, vegetation, and hydrothermal alteration type from ASTER satellite imagery with examples from the San Juan Mountains, Colorado: U.S. Geological Survey Scientific Investigations Map 3190, 5 sheets, scale 1:100,000, 35-p. pamphlet, accessed October 10, 2016 at https://doi.org/10.3133/sim3190.

Rockwell, B.W., 2013a, Automated mapping of mineral groups and green vegetation from Landsat Thematic Mapper imagery with an example from the San Juan Mountains, Colorado: U.S. Geological Survey Scientific Investigations Map 3252, 1 sheet, scale 1:325,000, 25-p. pamphlet, accessed October 10, 2016 at https://doi.org/10.3133/sim3252.

Rockwell, B.W., 2013b, Comparative mineral mapping in the Colorado Mineral Belt using AVIRIS and ASTER remote sensing data: U.S. Geological Survey Scientific Investigations Map 3256, 1 sheet, scale 1:150,000, 8-p. pamphlet, accessed October 10, 2016 at https://doi.org/10.3133/sim3256.

Rockwell, B.W., Bonham, L.C., and Giles, S.A., 2015, USGS National Map of Surficial Mineralogy: U.S. Geological Survey Online Map Resource, accessed October 25, 2016, at https://www.sciencebase.gov/arcgis/rest/services/usminmap.

Rockwell, B.W., and Gnesda, W.R., 2021, Digital map of iron sulfate minerals, other mineral groups, and vegetation of the western United States derived from automated analysis of Landsat 8 satellite data: U.S. Geological Survey data release, https://doi.org/10.5066/P9ONOKKX.

Rockwell, B.W., and Hofstra, A.H., 2008, Identification of quartz and carbonate minerals across northern Nevada using ASTER thermal infrared emissivity data-Implications for geologic mapping and mineral resource investigations in well-studied and frontier areas: Geosphere, v. 4, no. 1, p. 218–246, accessed October 10, 2016 at https://doi.org/10.1130/GES00126.1.

Rockwell, B.W., and Hofstra, A.H., 2012, Mapping argillic and advanced argillic alteration in volcanic rocks, quartzites, and quartz arenites in the western Richfield 1°×2° quadrangle, southwestern Utah, using ASTER satellite data: U.S. Geological Survey Open-File Report 2012–1105, 5 p., 1 plate, 2 geospatial PDF maps, accessed October 10, 2016 at https://doi.org/10.3133/ofr20121105.

Rockwell, B.W., McDougal, R.R., and Gent, C.A., 2005, Remote sensing for environmental site screening and watershed evaluation in Utah mine lands—East Tintic Mountains, Oquirrh Mountains, and Tushar Mountains: U.S. Geological Survey Scientific Investigations Report 2004–5241, 84 p., accessed October 10, 2016 at https://doi.org/10.3133/sir20045241.

Rye, R.O., Bethke, P.M., and Wasserman, M.D., 1992, The stable isotope geochemistry of acid sulfate alteration: Economic Geology and the Bulletin of the Society of Economic Geologists, v. 87, p. 225–262, accessed October 10, 2016 at https://doi.org/10.2113/gsecongeo.87.2.225.

Schmidt, T.S., Church, S.E., Clements, W.H., Mitchell, K.A., Fey, D.L., Wanty, R.B., Verplanck, P.L., San Juan, C.A., DeWitt, E.H., Rockwell, B.W., and Klein, T.L., 2009, Aquatic ecosystems in central Colorado are influenced by mineral forming processes and historical mining: *in* Webb, R.M.T., and Semmens, D.J., eds., Planning for an uncertain future—Monitoring, integration, and adaptation. Proceedings of the Third Interagency Conference on Research in the Watersheds: U.S. Geological Survey Scientific Investigations Report 2009–5049, 292 p., accessed October 10, 2016 at https://doi.org/10.3133/sir20095049.

Schmidt, T.S., Clements, W.H., Wanty, R.B., Verplanck, P.L., Church, S.E., San Juan, C.A., Fey, D.L., Rockwell, B.W., Dewitt, E.H., and Klein, T.L., 2012, Geologic processes influence the effects of mining on aquatic ecosystems: Ecological Applications, v. 22, no. 3, p. 870–879 accessed October 10, 2016 at https://doi.org/10.1890/11-0806.1.

Schmitt, L.J., and Raymond, W.H., 1977, Geology and mineral deposits of the Needle Mountains district, southwestern Colorado: U.S Geological Survey Bulletin 1434, 40 p. [Also available at https://doi.org/10.3133/ofr76244.]

Seal, R.R., II, and Foley, N.K., eds., 2002, Progress on geoenvironmental models for selected mineral deposit types: U.S. Geological Survey Open-File Report 02-195, 217 p., accessed October 10, 2016 at https://pubs.usgs.gov/of/2002/of02-195/.

Song, C., Woodcock, C.E., Seto, K.C., Lenney, M.P., and Macomber, S.A., 2001, Classification and change detection using Landsat TM data—When and how to correct atmospheric effects: Remote Sensing of Environment, v. 75, p. 230–244, accessed October 10, 2016 at https://doi.org/10.1016/S0034-4257(00)00169-3.

Swayze, G.A., Clark, R.N., Goetz, A.F.H., Livo, K.E., Breit, G.N., Kruse, F.A., Sutley, S.J., Snee, L.W., Lowers, H.A., Post, J.L., Stoffregen, R.E., and Ashley, R.P., 2014, Mapping advanced argillic alteration at Cuprite, Nevada, using imaging spectroscopy: Economic Geology and the Bulletin of the Society of Economic Geologists, v. 109, p. 1179–1221, accessed August 3, 2016 at https://doi.org/10.2113/econgeo.109.5.1179.

U.S. Geological Survey, 2013, What are the band designations for the Landsat satellites?: U.S. Geological Survey web page, accessed October 25, 2016, at https://www.usgs.gov/faqs/what-are-band-designations-landsat-satellites?qt-news_science_products=0#qt-news_science_products.

Vikre, P.G., Benson, M.E., Bleiwas, D.I., Colgan, J.P., Cossette, P.M., DeAngelo, J., Dicken, C.L., Drake, R.M., II, du Bray, E.A., Fernette, G.L., Glen, J.M.G., Haacke, J.E., Hall, S.M., Hofstra, A.H., John, D.A., Ludington, S., Mihalasky, M.J., Rytuba, J.J., Shaffer, B.N., Stillings, L.L., Wallis, J.C., Williams, C.F., Yager, D.B., and Zürcher, L., 2016, Geology and mineral resources of the Sheldon-Hart Mountain National Wildlife Refuge Complex (Oregon and Nevada), the Southeastern Oregon and North-Central Nevada, and the Southern Idaho and Northern Nevada (and Utah) Sagebrush Focal Areas (ver. 1.1, October 28, 2016): U.S. Geological Survey Scientific Investigations Report 2016–5089–B, 224 p., accessed October 10, 2016 at https://doi.org/10.3133/sir20165089B.

Vincent, R.K., 1997, Fundamentals of Geological and Environmental Remote Sensing 1st ed.: Upper Saddle River, N.J., Prentice Hall, 370 p.

Yager, D.B., Choate, L., and Stanton, M.R., 2008, Net acid production, acid neutralizing capacity, and associated mineralogical and geochemical characteristics of Animas River watershed igneous rocks near Silverton, Colorado: U.S. Geological Survey Scientific Investigations Report 2008–5063, 63 p., accessed October 10, 2016 at https://doi.org/10.3133/sir20085063.

Publishing support provided by the Science Publishing Network,
Denver and Lafayette Publishing Service Centers

For more information concerning the research in this report, contact the
Center Director, USGS Geology, Geophysics, and Geochemistry Science Center
Box 25046, Mail Stop 973
Denver, CO 80225
(303) 236-1800

Or visit Geology, Geophysics, and Geochemistry Science Center website
at https://www.usgs.gov/centers/gggsc

ISSN 2329-132X (online)
https://doi.org/10.3133/sim3466